# Analysis of brain and blood single-cell transcriptomics in acute and subacute phases after experimental stroke

Lidia Garcia-Bonilla ⬤ ✉, Ziasmin Shahanoor, Rose Sciortino, Omina Nazarzoda ⬤ , Gianfranco Racchumi, Costantino Iadecola ⬤ & Josef Anrather ⬤ ✉

Cerebral ischemia triggers a powerful inflammatory reaction involving peripheral leukocytes and brain resident cells that contribute to both tissue injury and repair. However, their dynamics and diversity remain poorly understood. To address these limitations, we performed a single-cell transcriptomic study of brain and blood cells 2 or 14 days after ischemic stroke in mice. We observed a strong divergence of post-ischemic microglia, monocyte-derived macrophages and neutrophils over time, while endothelial cells and brain-associated macrophages showed altered transcriptomic signatures at 2 days poststroke. Trajectory inference predicted the in situ trans-differentiation of macrophages from blood monocytes into day 2 and day 14 phenotypes, while neutrophils were projected to be continuously de novo recruited from the blood. Brain single-cell transcriptomes from both female and male aged mice were similar to that of young male mice, but aged and young brains differed in their immune cell composition. Although blood leukocyte analysis also revealed altered transcriptomes after stroke, brain-infiltrating leukocytes displayed higher transcriptomic divergence than their circulating counterparts, indicating that phenotypic diversification occurs within the brain in the early and recovery phases of ischemic stroke. A portal (https://anratherlab.shinyapps.io/strokevis/) is provided to allow user-friendly access to our data.

The immune system actively participates in the acute and chronic pathogenesis of ischemic stroke. Damaged neurons lead to a secondary inflammatory reaction that aggravates brain injury, increasing neurologic deficits[1]. This response progresses for days to weeks and involves glial and brain endothelium activation and recruitment of peripheral immune cells. Although there is evidence that the acute inflammatory response contributes to the progression of ischemic brain injury, more recent research points to a more multifaceted role of immune cells in brain ischemia, whereby they participate in repair processes during the subacute and chronic stages[2-4]. Emerging single-cell RNA sequencing (scRNA-seq) studies reveal a high cellular heterogeneity in the response to ischemic stroke[5-10], supporting the functional plasticity of brain and immune cells after stroke. Furthermore, the ischemic brain and systemic immunity interact in a bidirectional fashion. While the immune system supplies the brain with immune cells that participate in the local inflammatory response, neural and humoral factors generated by the

ischemic brain communicate to peripheral organs[1]. Thus, activation of the immune system through brain-derived molecules or by the autonomic nervous system might lead to the transcriptional differentiation of immune cells before entering the brain. Here, we used scRNA-seq to gain deeper insights into the impact of ischemic stroke on the transcriptional diversity of brain immune cells, endothelial cells (ECs) and peripheral blood leukocytes. Specifically, this study focuses on assessing differences in transcriptomic signatures related to cell origin (brain resident vs recruited cells), cellular localization (periphery vs brain) time post stroke (acute vs subacute) and age (young vs aged mice).

## Results

### Brain and blood cell heterogeneity over the ischemic–reperfusion time

We prepared brain single-cell suspensions from young male mice 2 days after sham surgery (Sham) or 2 and 14 days after stroke (D02 and D14, respectively; Extended Data Fig. 1a) and flow-sorted CD45^{hi} cells, microglia and ECs (Supplementary Fig. 1). Droplet-based scRNA-seq revealed 13 distinct major cell clusters in 43,269 cells after performing unsupervised clustering and uniform manifold approximation and projection (UMAP). Based on the expression of established marker genes and unsupervised cell type annotation, clusters were identified as microglia, border-associated macrophages (BAMs), myeloid-derived cells (MdCs), granulocytes, mast cells, dendritic cells (DCs), T cells, natural killer (NK) cells, B cells, ECs, vascular mural cells, epithelial-like cells and oligodendrocytes (Extended Data Fig. 1b and Supplementary Fig. 3b). As anticipated, we observed that the relative abundance of each cell cluster changed notably with ischemia–reperfusion. For instance, MdCs increased at D02, whereas the increase in lymphocytes (T cells and NK cells) was more pronounced at D14, as previously reported[11,12]. Amid brain resident cells, we observed divergent clustering of microglia across Sham, D02 and D14, indicating that ischemic injury markedly modified microglial transcriptomes. On the other hand, less heterogeneity was observed in BAMs and ECs (Extended Data Fig. 1b).

Given that brain ischemia elicits a systemic immune response that ultimately affects stroke outcome[1], we next sought to explore the transcriptomes of peripheral blood cells from stroke mice. scRNA-seq of blood leukocytes from Sham, D02 and D14 mice identified nine distinct clusters that were annotated by the expression of commonly used marker genes as follows: monocytes, neutrophils, eosinophils–basophils, DCs, T cells, NK cells, B cells, various precursors and one unclassified cluster (Extended Data Fig. 1c and Supplementary Fig. 4b). Overall, the major peripheral blood immune cell types showed conserved positioning in the UMAP space across conditions. Only granulocyte and monocyte clusters were slightly divergent at D14 from their respective Sham and D02 clusters. Thus, these results point to lesser phenotypic differentiation in circulating leukocytes than in brain-recruited leukocytes after stroke.

Combined analysis of brain and blood datasets showed that non-brain resident immune cells clustered together independently of

their tissue origin. Conversely, the microglia cluster remained spatially separated from blood myeloid cells, reflecting their unique transcriptome (Extended Data Fig. 1d).

### Transcriptomic states of microglia at different phases after stroke

To determine whether distinct transcriptional programs of microglia develop over the ischemia–reperfusion time, we re-clustered microglia, which resulted in eight clusters (Mg1–Mg8), all showing high expression of canonical microglial markers *Hexb*, *Olfml3* and *Fcrls* (Fig. 1a–d and Supplementary Fig. 5b). Sham microglia mostly fell into clusters Mg1 and Mg2. Mg1 was characterized by the expression of homeostatic genes (*Siglech*, *P2ry12*, *Tmem119*), whereas Mg2 showed upregulation of immediate early genes (*Jun*, *Fos*, *Erg1*, *Klf2*, *Klf4* and *Atf3*), a group of transcription factors that are typically expressed in microglia of adults and are involved in establishing microglia surveilling functions[13]. In line with recent reports, we observed that microglial homeostatic genes (*P2ry12*, *Tmem119*) were downregulated after ischemia[6,14] (Fig. 1b). The expression of *Apoe*, *Lpl*, *Spp1*, *Clec7a* or *Cst7* genes, which have been linked to microglial responses to demyelination[15], Alzheimer's disease[16] and stroke[6,14], were upregulated in both D02 and D14 microglia (Fig. 1a–d). Furthermore, cerebral ischemia led to distinct D02 and D14 microglia clusters. D02 microglia mainly comprised Mg4 and Mg5 clusters, while the most prominent clusters at D14 were Mg3, Mg6 and Mg7 (Fig. 1c). Mg4 showed high expression of genes related to the clearance of damaged cells and tissue repair (*Spp1*, *Msr1* and *Lgals3*)[14,17], and high expression of chemokine genes (*Ccl2*, *Ccl12*). The Mg5 cluster showed expression of mitotic genes including *Top2A*, *Mki67* and *Stmn1*[10], indicating microglia proliferation during the acute phase of stroke. Mg3, the predominant cluster at D14, was defined by genes affiliated with disease-associated microglia (DAM), including *Apoe*, *Cst7*, *Clec7a*, *Lyz2*, *Lgals3bp*, *Igf1* and *Lpl*[16] (Supplementary Fig. 5c). Similar to Mg3, Mg7 was characterized by DAM genes (*Spp1*, *Apoe*, *Cst7*, *Igf1*, *Lgals3bp*, *Apoc1*, *Lpl*, *Gpnmb*, *Itgax*)[16] and by expression of genes observed in the response of microglia to neurodegeneration (*Gpnmb*, *Axl*, *Itgax*, *Spp1*, *Apoe*)[18]. Mg6 showed upregulation of immune genes (*Il1b*, *Nfkbiz*, *Cd83*, *Ccl4*) and genes of disease inflammatory macrophages/microglia (DIM; *Il1b*, *Cd83*, *Nfkbiz*, *Atf3*, *Ccl4*, *Egr1*, *Fosb*)[19] (Supplementary Fig. 5c). Pseudotime trajectory predicted the progression of Sham microglia (Mg1) to either D02 or D14 microglia, whereas we could not observe a trajectory from D02 to D14 microglia (Fig. 1e).

Given that microglia undergo significant morphological and functional differentiation after cerebral ischemia, which could confound discrimination from infiltrating MdCs[20], we used tamoxifen-inducible *Cx3cr1*-Td mice to distinguish brain resident from hematopoietic myeloid cells[21]. We subjected *Cx3cr1*-Td mice that had been injected with tamoxifen 6–8 weeks earlier to Sham, D02 or D14 stroke and performed scRNA-seq on Td^{+} brain cells sorted by flow cytometry. Unsupervised annotation using the wild-type brain dataset as a reference showed that the majority of *tdTomato*-expressing cells were annotated as

---

**Fig. 1 | Microglia show altered transcriptional states through the acute and subacute phases of stroke. a**, Left panel: UMAP of merged Sham, D02 and D14 microglial single-cell transcriptomes reveals eight clusters; right panel: UMAP of overlaid time points reveals high segregation of microglial clusters among Sham, D02 and D14 groups. **b**, Feature plots depicting single-cell gene expression of individual genes characterizing homeostatic and activated microglia. Scale bars represent log normalized gene expression. **c**, Bar graph showing relative frequencies of each cluster across Sham, D02 and D14 groups. **d**, Heatmap displaying expression of the top ten upregulated genes in each microglial cluster. Scale bar represents *z*-score of average gene expression (log). **e**, Pseudotime analysis of microglial clusters showing transitional trajectories from Sham Mg1 cluster to either Sham–Mg2, or D02 Mg4–Mg5 clusters, or D14 Mg3, Mg6–Mg7 clusters. **f**, Representative fluorescence images of the cerebral hemisphere after Sham surgery or at D02 or D14 after MCAo in *Cx3cr1*[CreERT2]:R26tdTomato

mice. Microglia were identified as Td^{+} cells (red). Images show that the number of microglia decreased in the ischemic core (white dashed outline) at D02 whereas its number increased at D14. **g**, UMAPs of individual marker genes that characterize ischemic microglial clusters. Scale bars represent log normalized gene expression. **h**, Diagram of a brain coronal section indicating anatomical regions where the images in **i–m** were acquired. **i**, Immunofluorescence images showing Ki67 (white) expression by *Cx3cr1*-Td[+] (red) Iba1^{+} (blue) microglia 2 days after MCAo. Arrowheads indicate Ki67 staining. **j**, RNAscope FISH and IF images validating *Cst7* (white) expression in D02 *Cx3cr1*-Td[+] microglia (Td[+], red); nuclei are DAPI[+] (blue). **k,l**, FISH images showing *Cxcl10* (white) expression in D02 (**k**) and D14 (**l**) *Cx3cr1*-Td[+] microglia (Td[+], red); nuclei are DAPI[+] (blue). **m**, IF images showing IGF1 (white) expression by *Cx3cr1*-Td[+] (red) MHCII[−] (green) microglia 14 days after MCAo.

microglia (92.7%) followed by BAMs (2.9%), MdCs (2.0%) and DCs (1.3%) (Supplementary Fig. 5d).

To spatially map major microglia clusters, we examined the brains of *Cx3cr1*-Td stroke mice by histology and fluorescence in situ hybridization–immunofluorescence (FISH–IF) (Fig. 1f). We observed that

*Cx3cr1*-Td⁺ cells were significantly reduced in the ischemic core at D02 but rebounded at D14 (Fig. 1f). We observed colocalization of *Cx3cr1*-Td⁺Iba1⁺ microglia with the mitotic marker Ki67 at the infarct border at D02 (Fig. 1i and Extended Data Fig. 2a), suggesting that proliferative microglia contribute to the repopulation of the ischemic territory seen at D14.
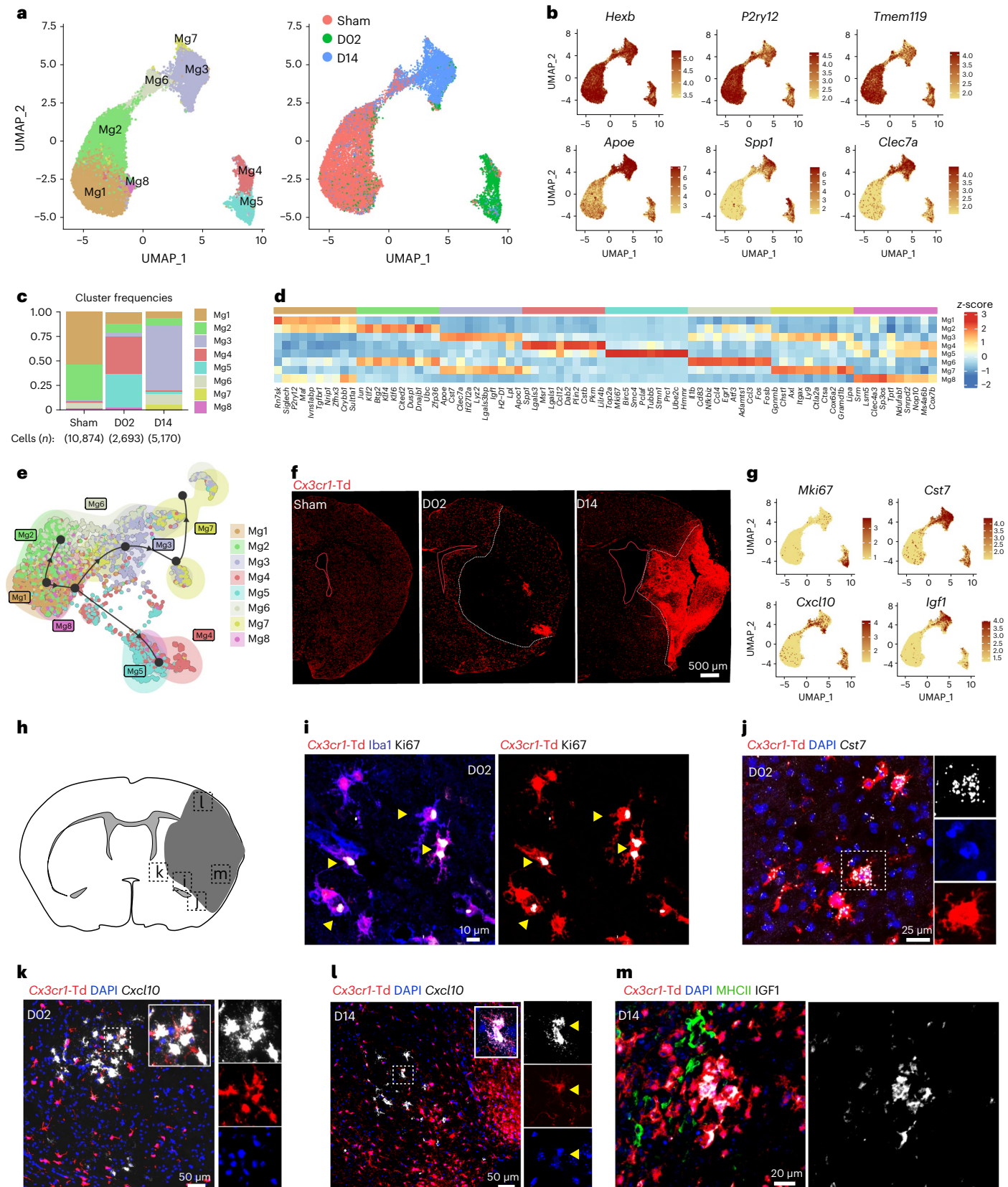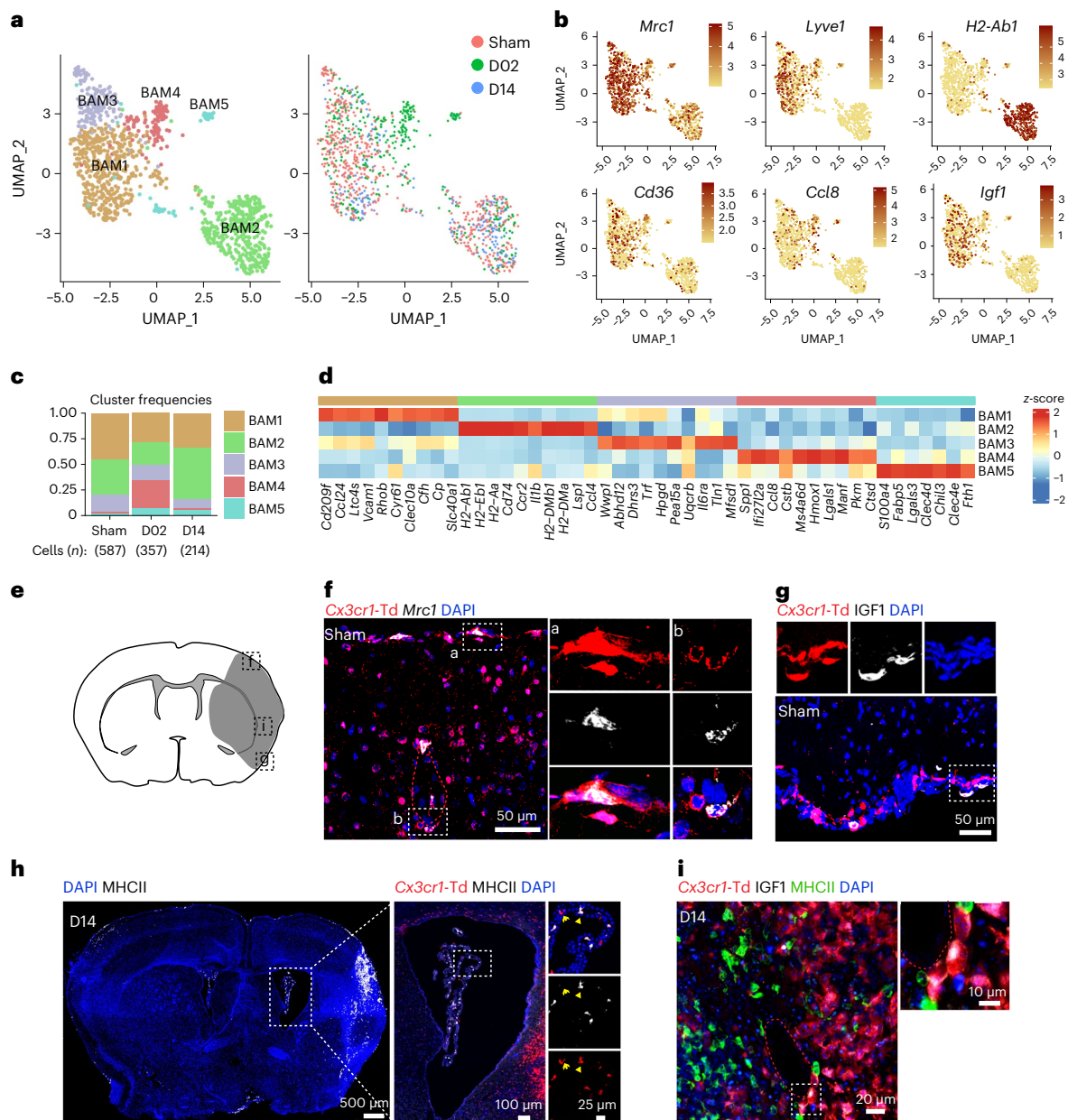
**Fig. 2 | Transcriptional changes of BAMs after stroke. a**, UMAP analysis of merged Sham, D02 and D14 BAM transcriptomes showed five clusters (left panel); UMAP of overlaid time points reveals overlapping clusters among Sham, D02 and D14 groups, except for BAM4, which is confined to D02 (right panel). **b**, UMAP plots depicting expression of individual marker genes for BAM (*Mrc1*, *Cd36*), meningeal and perivascular BAM (*Lyve1*), choroid plexus BAM (*H2-Ab1*) and activated meningeal and perivascular BAM (*Ccl8*, *Igf1*). Scale bars represent log of normalized gene expression. **c**, Bar graph showing relative frequencies of BAM clusters across Sham, D02 and D14 groups. **d**, Heatmap displaying expression of the top ten upregulated genes in each BAM cluster. Scale bar represents *z*-score of average gene expression (log). **e**, Graphical representation of brain coronal section indicating anatomical regions where the images in **f–i** were acquired. **f**, RNAscope FISH images of brain cortical areas showing *Mrc1* expression (white) in resident macrophages (Td+, red) on the brain surface and around vessels of *Cx3cr1*-Td+ mice 2 days after Sham surgery (Sham). Nuclei are stained with DAPI (blue). **g,i**, IF images validating IGF1 (white) expression by pial BAM (Td+, red) (**g**) in Sham *Cx3cr1*-Td+ mice and in perivascular macrophages (**i**) of the ischemic brain at D14. **h**, Representative IF image of a whole brain section from a *Cx3cr1*-Td+ mouse subjected to 14 days of MCAo (D14), showing MHCII+ cells (white, binary mask) localization and nuclear DAPI staining (blue) (left panel); IF images of magnified areas of the choroid plexus showing MHCII expression (white) by ChMp (Td+, red) (right panel).

The DAM marker *Cst7* colocalized with ramified microglial cells at the infarct border and with ameboid cells in the ischemic core (Fig. 1j and Extended Data Fig. 2b), suggesting that cell morphology was not associated with a DAM signature. We also identified *Cxcl10* and *Igf1* among the differentially expressed genes (DEGs) that were upregulated in microglia after ischemia (Fig. 1g). Microglial induction of the inflammatory chemokine *Cxcl10*, an interferon (IFN) type I stimulated gene, has previously been reported in models of traumatic and ischemic brain injury, experimental autoimmune encephalomyelitis and Alzheimer's disease[14,22], while insulin-like growth factor 1 (IGF1) expressing microglia has been associated with a pro-neurogenic phenotype after stroke[23]. We observed that *Cxcl10* was upregulated at D02 and D14, whereas *Igf1* was mainly induced at D14 (Fig. 1g). By histology, we also found *Cxcl10*-expressing microglia in the infarct border at D02 and in the lesioned tissue at D14, while IGF1+ microglia were found in the ischemic core (Fig. 1k–m and Extended Data Fig. 2c–d). In some

instances, Td⁺Cxcl10⁺ microglia were found near Td⁻Cxcl10⁺ cells, suggesting that microglia and non-microglial cells expressing *Cxcl10* organize into discrete cell clusters (Fig. 1l).

## Altered transcriptional states in BAMs early after stroke

We identified five BAM clusters (Fig. 2a). BAM1 and BAM2 were the most abundant clusters in all groups (Fig. 2c). BAM1 showed the transcriptional signature of subdural BAMs (*Cd209f, Ccl24, Clec10a, Slc40a1, Stab1*)[24]. Some of these genes have been found in homeostatic BAMs and are related to leukocyte recruitment (*Ccl24*), phagocytosis (*Cd209f*) and iron metabolism (*Slc40a1, Cp*)[25]. BAM2 showed expression of canonical marker genes of choroid plexus macrophages (ChMp) such as major histocompatibility complex (MHC) class II genes (*H2-Ab1, H2-Eb1, H2-Aa, H2-DMb1, H2-DMa*) and low levels of the perivascular macrophage marker *Lyve1* (Fig. 2b,d)[24]. BAM3 (*Wwp1, Abhd12, Dhrs3, Hpgd, Trf*) was less frequent at D14, while BAM4 was largely confined to D02 and was characterized by genes linked to macrophage or microglia activation (*Spp1, Ccl8, Cstb, Lgals1*)[24,26]. BAM5 showed expression of genes related to lipid metabolism (*Fabp5, Lgals3*)[27] and damage-associated molecular pattern-recognition molecules (*S100A4, Lgals3, Clec4d, Clec4e*)[28].

Using *Cx3cr1*-Td mice, we mapped BAMs on the surface of the brain or lining parenchymal blood vessels by *Mrc1* (CD206) and Td co-detection. Consistent with the scRNA-seq data, MHC class II antigen was only detected in ChMp, whereas perivascular macrophages and pial macrophages expressed IGF1 (Fig. 3f–i).

## MdCs differentiate from inflammatory monocytes in the brain

Re-clustering of blood monocytes identified five clusters (Mo1–Mo5) (Fig. 3a). Based on *Ly6c2* and *Cd36* expression, monocyte clusters were annotated as inflammatory (Mo1, Mo2, Mo4 and Mo5; *Ly6c2* high, *Cd36* low) or patrolling (Mo3; *Ly6c2* low, *Cd36* high) monocytes[29] (Fig. 3b). Mo1 was most abundant at D14 and was characterized by increased expression of S100 proteins and chemokines (*S100a10, S100a4, Ccl9, Ccl6*). Conversely, Mo2 was predominant at D02 and exhibited a transcriptional profile of 'neutrophil-like' Ly6Cʰⁱ monocytes (*Saa3, Mmp8, Lcn2, Wfdc21, Lrg1, Chil3*)[30]. Furthermore, Mo4 showed an interferon-stimulated gene (ISG) signature (*Ifit3, Ifit2, Isg15, Ifi211, Ifi205, Ifit1bl1, Ifi203*) and Mo5 showed high expression of MHCII genes (*H2-Ab1, H2-Eb1, H2-Aa, H2-DMb1, H2-DMa*), resembling monocyte-derived DCs (MoDCs)[31]. In addition to *Cd36*, Mo3 expressed several genes characteristic of patrolling monocytes (*Ear2, Treml4, Eno3, Aceas*)[30] (Fig. 3c–d).

We identified six brain MdC populations. Sham brain displayed low numbers of MdCs and most of them (~75%) clustered as MdC3, a cluster closely related to blood monocytes (*Serpinb10, Plac8, Sell*) (Fig. 3e,f and Supplementary Fig. 6a,b). MdC1 and MdC2 were the predominant clusters at D02 and MdC6 was the major cluster at D14. MdC1 expressed a gene signature (*Fabp5, Spp1, Gpnmb, Ctsl, Cd63, Ctsb, Ctsd, Arg1*) that has been found in stroke-associated macrophages, foamy macrophages in atherosclerotic plaques and lipid-associated macrophages

in myocardial infarct (Fig. 3h and Supplementary Fig. 6b)[6,32,33]. MdC2 showed upregulation of neutrophil chemoattractants (*Cxcl1, Cxcl2, Cxcl3*) and other pro-inflammatory genes (*Ptgs2, Il1b, Clec4e*), suggesting a role in driving post-stroke inflammation. Like MdC1, MdC6 showed increased expression of genes characteristic of stroke-associated macrophages but differed from MdC1 by enrichment for the growth factor *Igf1*. MdC4 cells showed an ISG signature (Supplementary Fig. 6b), while MdC5 exhibited upregulation of MHCII-associated genes, identifying this cluster as moDC[31]. Trajectory analysis showed the sequential transition of inflammatory peripheral blood Mo1 and Mo2 clusters to brain MdC3 cluster, followed by MdC2, MdC4 and MdC1 transition and final differentiation into MdC6. MdC5 appeared as the only MdC cluster dissociated from the trajectory (Fig. 3f). This suggests that MdCs in the inflamed brain derive from inflammatory monocytes and that both MdC1 and MdC6 constituted bonafide tissue macrophages, while MdC2, MdC3 and MdC4 were clusters associated with transitional phenotypes.

*Spp1* and *Gpnmb* were preferentially upregulated in fully differentiated MdC1 and MdC6 clusters (Fig. 3h–i). Upregulation of these two genes in brain macrophages has been linked to tissue regeneration and neuroprotection after stroke[34,35]. MdC1 was characterized by *Arg1* expression, a gene associated with efferocytosis[36]. Detection of *Arg1* by combined FISH−IF revealed that *Arg1* increased at D02 in infiltrating macrophages (*Cx3cr1*-Td⁻ cells) located on the brain surface or structures resembling parenchymal blood vessels (Fig. 3j). In addition, we found upregulation of *Cxcl10* at both D02 and D14 (MdC4) and of *Igf1* at D14 (MdC6), similar to the one observed in microglia (Fig. 3k–m and Extended Data Fig. 2c–d). Many of the *Cxcl10*-expressing MdCs were organized in cell clusters together with *Cxcl10*-producing microglia, indicating that local environmental cues in selected brain regions might drive the ISG phenotype in MdCs and microglia.

## Lrg1 identifies reactive endothelium early after stroke

ECs segregated into nine subclusters (EC1–EC9), which, by marker gene expression, could be attributed to four arteriovenous segments (Fig. 4a–c): EC1 (venous capillaries; *Car4, Tfrc*), EC6 (large veins; *Vcam1, Cfh, Scl38a5*), EC3 (arterial capillaries; *Fos, Fosb*), EC4 (arteries; *Gkn3, Mgp, Stmn2, Bmx*) and EC7 (arteries; *Clu, Cdh13, Mgp, Stmn2, Bmx*)[37]. EC2, EC6 and EC9, which clustered together in the UMAP space, showed upregulation of the endothelial venule marker *Lrg1*, a gene associated with angiogenesis after ischemic stroke[38]. In addition, EC6 was defined by high gene expression of the venular atypical chemokine receptor *Ackr1* (ref. 39), lipocalin 2 (*Lcn2*), which has been implicated in stroke injury[40] and, consistent with a venous phenotype, adhesion molecules *Icam1* and *Vcam1*. Attesting to their reactive state, EC2, which was the predominant cluster at D02 (Fig. 4d), was defined by expression of *Ecscr*, a gene related to EC migration and vessel formation[41], *Anxa2* and *S100a11*, implicated in endothelial fibrinolysis[42], and *Scgb3a1*, an endothelial secreted protein crucial for tumor metastasis[43]. EC9 was characterized by genes involved in EC metabolic reprogramming

---

**Fig. 3 | Inflammatory blood monocytes give rise to infiltrating brain MdCs after stroke. a**, UMAP plot of blood monocytes in Sham or D02 and D14 after MCAo. **b**, UMAP plots depicting expression of marker genes *Cd36* (patrolling monocytes), *Ly6c2* (inflammatory monocytes) and *Ccr2* (pan-monocyte). Scale bars represent log normalized gene expression. **c**, Bar graph showing relative frequencies of monocyte clusters across treatment groups. **d**, Heatmap of the top ten upregulated genes in each monocyte cluster. Scale bar represents z-score of average gene expression (log). **e**, UMAP plot of brain MdCs across groups. **f**, Trajectory analysis of peripheral blood (PB) monocyte and brain (Br) Mdc subclusters. Each point is a cell and is colored according to its cluster identity shown in **a** and **e**. The inferred trajectory shows the transition from blood inflammatory monocyte clusters Mo1 and Mo2 to fully differentiated brain macrophages MdC1 and MdC6. **g**, Bar graph showing relative frequencies of MdC clusters across treatment groups. **h**, Heatmap of the top ten upregulated genes

in each MdC cluster. Scale bar represents z-score of average gene expression (log). **i**, UMAP plots of marker genes for each MdC cluster. Scale bars represent log normalized gene expression. **j**, FISH−IF image of *Arg1* (white) expression in *Cx3cr1*-Td⁺ mice D02 after stroke. Top panel, left: *Arg1* expression (binary mask) in a whole brain section co-stained for DAPI (blue). Top panel, right and bottom: images of magnified areas *a* and *b* showing localization of *Arg1* in *Cx3cr1*-Td⁻ and MHCII⁻ cells. Bottom panel, right: orthogonal projection showing *Arg1* expression in an adjacent cell to a perivascular macrophage (Td⁺, red). **k**, Diagram of a coronal brain section indicating regions where the images in **l** and **m** were acquired. **l**, FISH−IF images of *Cxcl10* expression (white) in MdC (Td⁻, F4-80⁺ cells, yellow arrow) and microglia (Td⁺, red; F4-80⁺, green) of D14 *Cx3cr1*-Td⁺ mice; nuclei are DAPI⁺ (blue). **m**, IF images in D14 *Cx3cr1*-Td⁺ mice showing IGF1 expression (white) in MdC (Td⁻, F4-80⁺, green) and microglia (Td⁺, red).
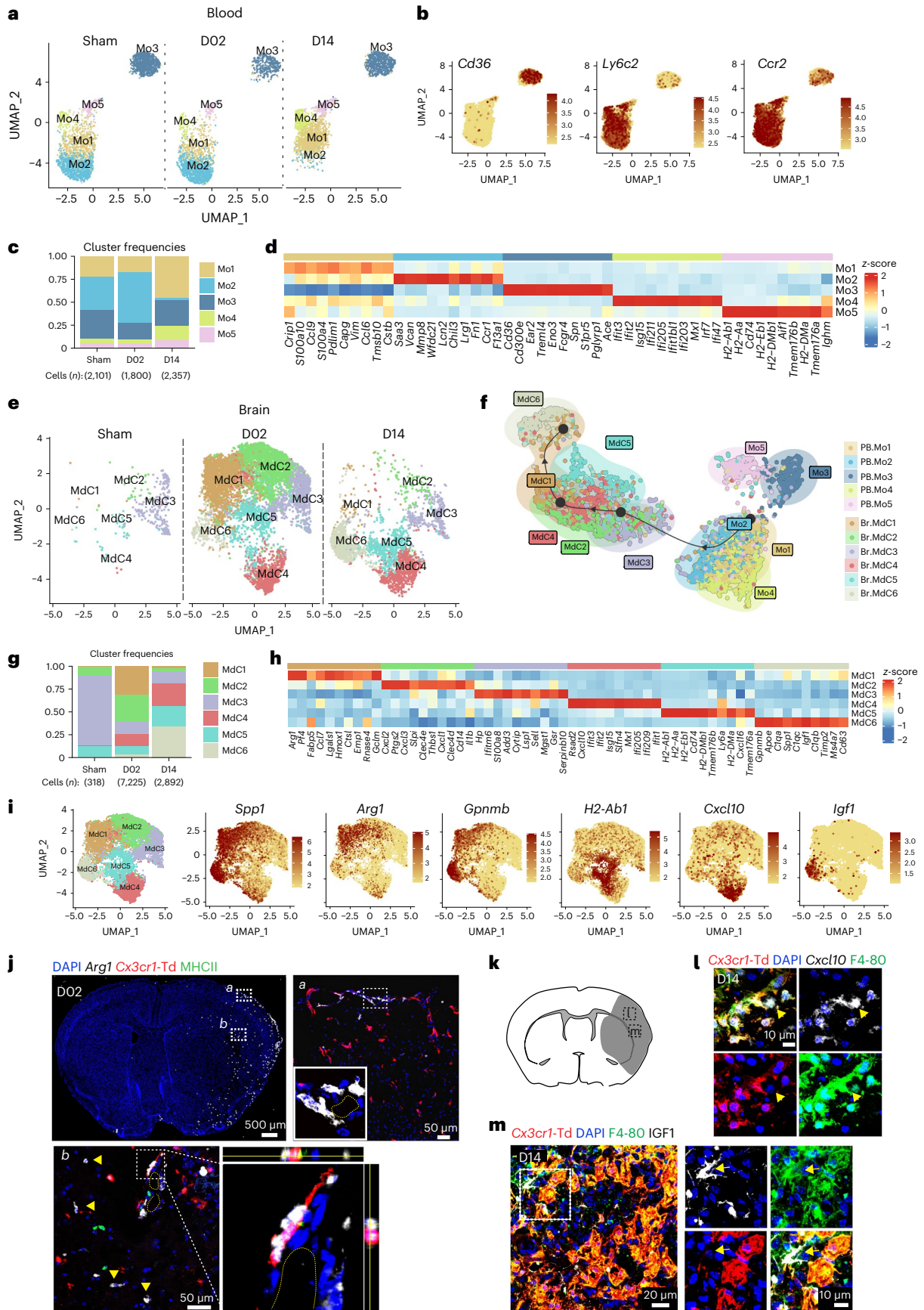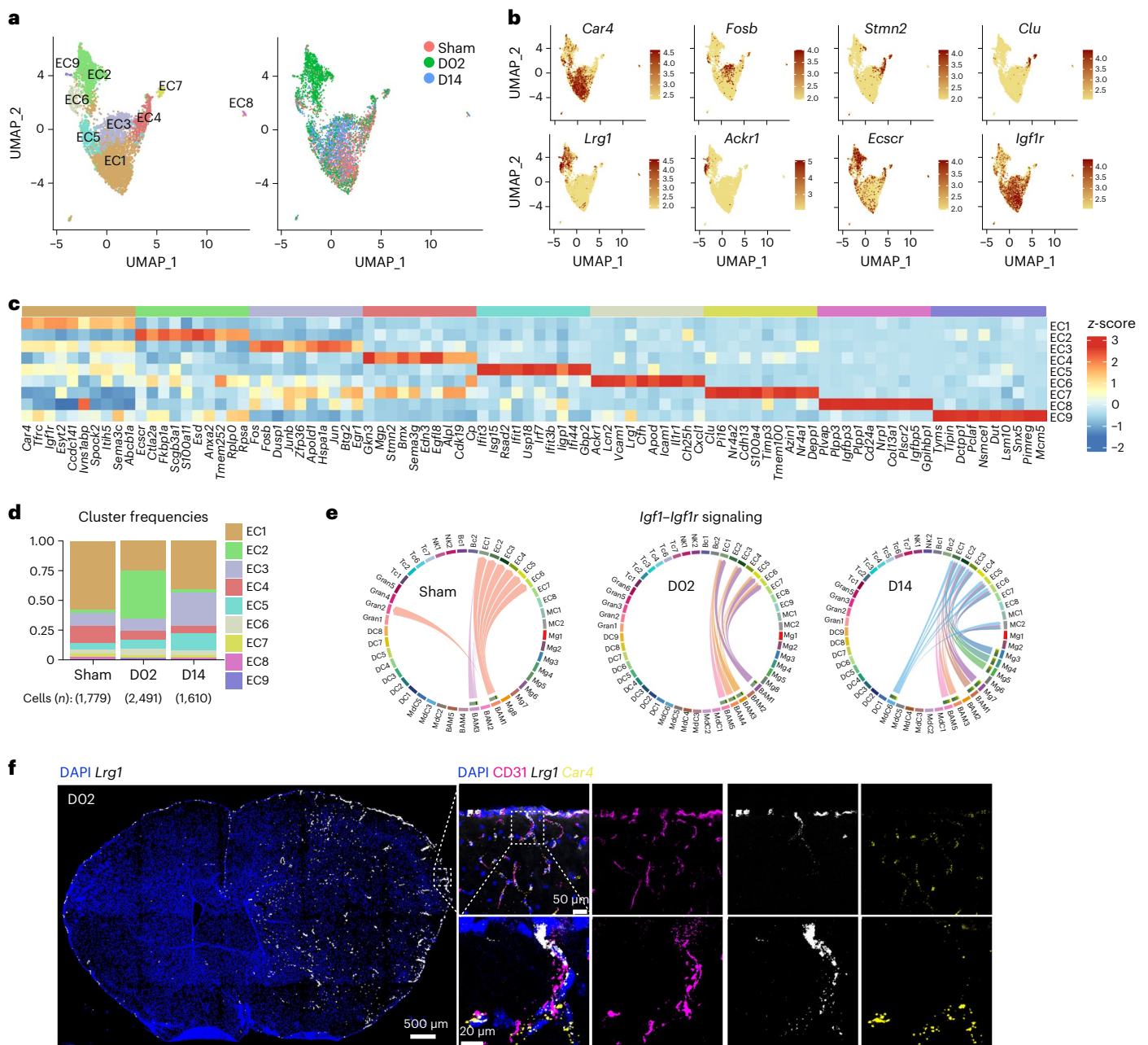
**Fig. 4 | EC transcriptional changes and *Igf1r* signaling after stroke. a**, Left panel: UMAP analysis of merged Sham, D02 and D14 EC transcriptomes identifies nine clusters; right panel: UMAP of overlaid time points shows dissociation of EC2 cluster at D02 and general overlap of all the other clusters across Sham, D02 and D14 groups. **b**, UMAP plots depicting single-cell gene expression of individual marker genes for capillary (*Car4*, *Fosb*), arterial (*Stmn2*, *Clu*) and venular (*Lrg1*, *Ackr1*) ECs and for the endothelial receptors *Ecscr* and *Igf1r*. Scale bars represent log of normalized gene expression. **c**, Heatmap displaying scaled differential expression of the top ten upregulated genes in each EC cluster. Scale bar represents z-score of average gene expression (log). **d**, Bar graph showing relative frequencies of EC clusters across Sham, D02 and D14 groups. **e**, Chord plots showing CellChat inferred ligand–receptor interactions between *Igf1r* and *Igf1* in Sham, D02 and D14 stroke mice. The strength of the interaction is indicated by the edge thickness. The color of the chord matches the cell cluster color sending the signal (*Igf1*). The number of cell recipient clusters (*Igfr1*) and their weight in the interactions is indicated by the color-matched stacked bar next to each sender. **f**, RNAscope FISH combined with IF of *Lrg1*. Left panel: overview of *Lrg1* expression (binary mask, white) in a D02 whole brain section co-stained for DAPI (blue), showing high upregulation of *Lrg1* in the ischemic hemisphere Right panel: magnified images of brain cortical areas showing *Lrg1* (white) colocalization with the EC marker CD31 (magenta) but not with the capillary marker *Car4* (yellow). Nuclei are stained with DAPI (blue).

(*Tyms, Dut, Dctpp1*)[44] and proliferation (*Pimreg, Pclaf*). EC8 showed a signature of fenestrated brain vascular ECs, probably stemming from choroid plexus or circumventricular organ ECs (*Plvap, Plpp3, Igfbp3, Plpp1, Cd24a, Ldb2*)[45]. Moreover, EC5 displayed increased ISG expression (Fig. 4c). It has been reported that brain ECs express IFN type I inducible genes at homeostasis and that after stroke, ECs show reduced ISG expression[46]. Despite our data showing significant ISG scores in the

Sham group, they were further increased at 2 or 14 days after stroke (Supplementary Fig. 7). We also found that ECs, particularly EC1, EC3 and EC5, exhibited high *Igf1r* expression (Fig. 4b,c). *Igf1r* levels are elevated in brain ECs compared to peripheral tissues[47]. Given that we found *Igf1* expression in microglia, MdCs and BAMs, we performed CellChat analysis to investigate interactions between ECs and IGF1-producing cells. *Igf1–Igf1r* communication occurred between BAMs and ECs in the
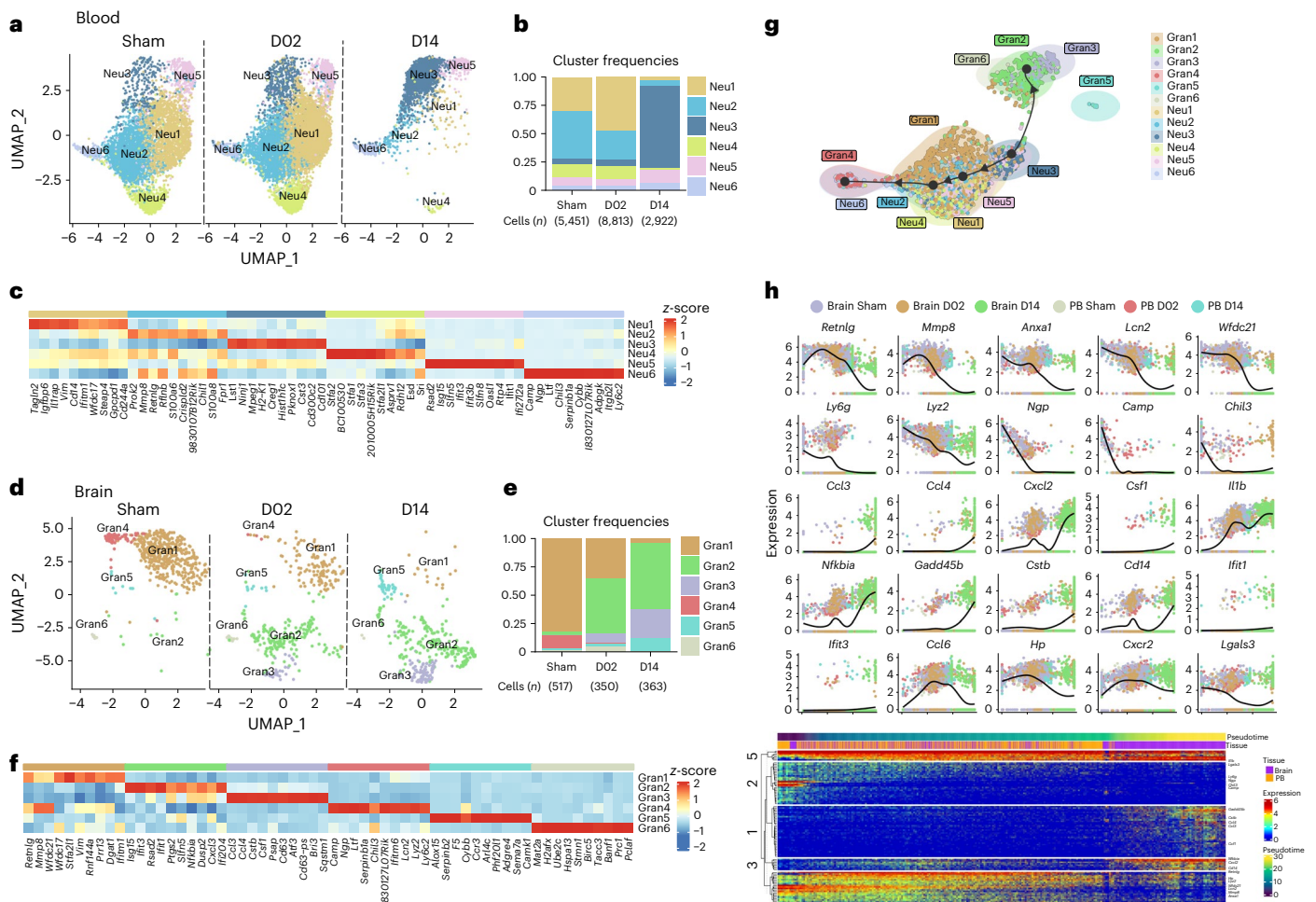
**Fig. 5 | Granulocyte transcriptional changes through ischemia–reperfusion. a,d**, UMAP plots of peripheral blood neutrophil (**a**) and brain granulocyte (**d**) transcriptomes by studied time point (Sham, D02, D14). Six clusters were identified in each dataset (Neu1–Neu6 and Gran1–Gran6, respectively). **b,e**, Bar graph showing relative frequencies of peripheral blood neutrophil (**b**) and brain granulocyte (**e**) clusters across Sham, D02 and D14 groups. **c,f**, Heatmap displaying differential expression of the top ten upregulated genes in each peripheral blood neutrophil (**c**) and brain granulocyte (**f**) cluster. Scale bars represent z-score of average gene expression (log). **g**, Slingshot trajectory of combined peripheral blood neutrophils and brain granulocytes showing predicted cluster transitions. Each point is a cell and is colored according to its cluster identity. **h**, Top panels: log normalized expression of single genes plotted as a function of pseudotime. Dot plots show expression levels of top cluster genes of combined peripheral blood neutrophil (PB) and brain granulocyte datasets along ischemic–reperfusion pseudotime. Each dot represents the expression levels (log) for each gene in a cell and is colored according to the group. Lines show the smoothed expression values obtained by generalized additive model fitting. Bottom panel: the top 100 genes that specifically covary with pseudotime were identified using generalized additive models and the log normalized expression values were plotted along the pseudotime axis. The location of genes plotted above is indicated.

Sham and D02 groups, whereas both microglia and MdC6 contributed to the *Igf1–Igf1r* signaling network at D14 (Fig. 4e).

FISH–IF analysis for the venule marker *Lrg1* (ref. 37) revealed strong upregulation of vascular *Lrg1* in the ischemic hemisphere (Fig. 4f). Co-detection of *Lrg1* and *Car4*, a marker for venule capillaries[37], showed low overlap between both markers, indicating that *Lrg1* was mainly induced in larger veins.

**Brain granulocytes are continuously recruited from the blood**
Blood neutrophils separated into six clusters (Neu1–Neu6) with similar frequencies in the Sham and D02 groups, whereas Neu3 became the predominant cluster at D14 (Fig. 5a–c). Neu1 showed increased expression of *Vim* and *Cd14*. Neu2 showed an immature Neu signature (*Mmp8, Retnlg, Lcn2, Ly6g*)[48] and the Neu4 cluster was enriched in stefinA family genes (*Stfa1, Stfa2, Stfa3, Stfa2l1, BC100530*), which are cytoplasmic inhibitors of proteases such as cathepsins[49]. On the other hand, Neu3, the predominant cluster at D14, was characterized by genes associated with neutrophil tissue infiltration (*Ninj1,*

*Cd300c2*)[50], cell growth inhibition (*Lst1, Creg1*) and markers of mature neutrophils (*Cd101*)[51].

We identified six brain granulocyte clusters (Gran1–Gran6) (Fig. 5d–f). Most of the Sham brain granulocytes fell into Gran1 and Gran4 clusters, which, similar to blood Neu2, were characterized by the upregulation of the immature neutrophil marker genes *Retnlg, Mmp8* and *Wfdc21* (ref. 48). In addition, Gran4 was specifically characterized by the induction of genes associated with early stage neutrophil development (*Camp, Ltf, Chil3, Lcn2*)[48]. We observed that Gran1 and Gran4 frequencies gradually decreased over the ischemia–reperfusion time, whereas the frequencies of Gran2, which showed upregulation of ISGs, and Gran3, characterized by the cytokine genes (*Ccl3, Ccl4, Csf1*) augmented progressively over D02 and D14. Furthermore, we detected two small clusters, Gran5, which also contained eosinophil markers (*Ccr3, Alox15*), and Gran6, which showed upregulation of the cell cycle genes *Pclaf, Banf1* and *Prc1*.

Trajectory analysis of combined blood neutrophils and brain granulocytes indicated similarities between Gran1, which is the major Sham

brain granulocyte cluster, and Neu1, Neu2 and Neu4, which were the main blood clusters at Sham and D02. On the contrary, Gran2 and Gran3 aligned closer to blood Neu3, the predominant blood granulocyte cluster at D14 (Fig. 5g). This analysis suggests that, in contrast to MdCs, granulocytes do not differentiate within the tissue but are recruited from the circulating pool at early and late phases after ischemia–reperfusion. We found that the pseudotime trajectory was characterized by the early expression of *Retnlg, Mmp8, Ly6g, Anxa1 and Lcn2* genes, top marker genes describing Sham brain granulocytes and Sham and D02 blood neutrophils. Conversely, late-expressed genes included *Ccl3, Ccl4, Csf1 and Gadd45b* in D14 brain granulocytes, suggesting different functions of brain neutrophils under homeostatic conditions and in the early and late phases of ischemic injury (Fig. 5h).

### Transcriptional changes in DCs

We identified nine DC subclusters in the brain. Low numbers of DCs were found in the brains of Sham mice, which gradually increased over the ischemia–reperfusion time (Extended Data Fig. 3a,b). Expression signatures of the clusters were related to the five main DC populations based on canonical markers: conventional cDC1 (*Xrc1, Clec9a*) and cDC2 (*CD209a, Sirpa* (CD172a)), the plasmacytoid DC (*Siglech, Ccr9, Bst2*), a subpopulation with high *Ccr7* and *Fscn1* expression representing migratory DCs (migDCs), and moDCs (*Ms4a7, Lyz2*)[24] (Extended Data Fig. 3c–e). We confirmed by flow cytometry the presence of DC (CD45$^{hi}$F480$^-$Lin$^-$CD11c$^+$MHCII$^+$) subtypes cDC1 (XCR1$^+$), cDC2 (CD172a$^+$ and CD209a$^+$) and migDC (CCR7$^+$) in the ischemic brain (Extended Data Fig. 3f). cDC1 comprised clusters DC2 and DC9. DC2 showed upregulation of *Irf8* transcription factor, which is required for the full development of cDC1 (ref. 52), whereas DC9 additionally showed a transcriptional signature of cDC1 dividing cells (*Lig1, Top2a, Mki67, Pcna*). cDC2, the largest population of brain DCs, comprised DC1, DC3, DC6 and DC7 clusters. DC1, the cDC2 cluster displaying the highest frequency at D14, showed upregulation of genes associated with antigen presentation (*Cd72, H2-Oa, H2-DMb2*), while DC7 showed expression of scavenger receptors (*Clec4b1, Mrc1, Cd209a*). DC4 exhibited high expression of monocyte and macrophage marker genes (*Lyz2, Csf1r, Apoe*, C1q genes, *Ms4a7, Trem2, and Cd14*), identifying them as moDCs[31], and DC6 was characterized by the upregulation of ISGs. migDCs were composed of a single subcluster (DC5) which, in addition to *Ccr7*, expressed other genes characteristic for migDCs including *Fscn1, Tmem123, Ccl22* and *Socs2* (ref. 24). DC8 classified as plasmacytoid DCs based on the expression of *Ccr9, Bst1, Il3ra, Siglech, Irf7, Ly6d*[24] (Extended Data Fig. 3e). Blood DCs were sparse (Extended Data Fig. 1b), and subclustering identified five clusters that corresponded to cDC2 (DC1, DC4), moDCs (DC2, DC3) and plasmacytoid DCs (DC5) by canonical marker annotation (Supplementary Fig. 8).

### Transcriptional changes in lymphoid cells

Brain-associated T cells split into seven clusters (Tc1–Tc7) (Extended Data Fig. 4a). T cells were more numerous at D14 than at Sham and D02 (Extended Data Fig. 4b). Expression of *Cd3d* identified all but one cluster (Tc6) as bonafide T cells. Tc6 classified as type 2 innate lymphoid cells (ILC2) based on the expression of *Il1rl1, Gata3, Areg* and *Calca*[53] (Extended Data Fig. 4c,e). Tc1 expressed *Cd4* (Extended Data Fig. 4e) and showed high *S1pr1* and *Klf2* expression (Extended Data Fig. 4c), consistent with a low activation and differentiation state[54]. Tc2 expressed features of cytotoxic T cells including *CD8b1* and several killer cell lectin-like receptors, suggesting that the cluster was composed of conventional CD8 and NK T cells. Cluster Tc3 was defined by an ISG signature and included CD8 as well as CD4 T cells (Extended Data Fig. 4c,e). This cluster was expanded at D14 after stroke, indicating increased IFN signaling during the subacute phase of ischemic injury (Extended Data Fig. 4b). Of note, CellChat analysis showed Tc2 and Tc3 cells interacting with Mg5, Mg6, BAM2, MdC4 and DC6 through the *Cxcr3–Cxcl10* pathway at D14, indicating that myeloid

*Cxcl10*-expressing cells might have a role in the recruitment of CD8$^+$ T cells into the brain[55] (Extended Data Fig. 4f). Tc4 expressed T cell receptors of the γδT cell lineage (*Trdc, Trdv4, Tcrg-C1*). Expression of *Il17a*, a cytokine that has been implicated in aggravating stroke pathology[56], was confined to the Tc4 cluster, suggesting that γδT and not T$_H$17 are the major IL-17-producing T cells after ischemic brain injury. Cluster Tc5 showed features of regulatory T cells (T$_{reg}$) including the expression of the canonical transcription factors *Foxp3* and *Ikzf2* (also known as HELIOS). Interestingly, cells in this cluster expressed TNF receptors *Tnfrsf4, Tnfrsf9* and *Tnfrsf18*, which have been found in non-lymphoid-tissue T$_{reg}$ cells but not in lymphoid-tissue-associated T$_{reg}$ cells[57], possibly indicating that brain-associated T$_{reg}$ cells do not originate from lymphoid organs such as lymph nodes or spleen but rather are recruited from non-lymphoid tissues or develop locally as previously suggested[4]. Similar to Tc3 and consistent with previous studies addressing T$_{reg}$ kinetics after ischemic brain injury[4], Tc5 was expanded at D14 after stroke (Extended Data Fig. 4a,b). Cluster Tc7 was characterized by the expression of cell proliferation markers including *Mki67, Top2a* and *Birc5*, consistent with the presence of in situ T cell proliferation, which was, however, not changed by stroke (Extended Data Fig. 4b,c). No major changes were observed in the longitudinal composition of blood T cells (Supplementary Fig. 9).

Similar to T cells, brain NK cells were increased at the D14 time point and could be separated into two clusters (Supplementary Fig. 10a,b). Brain NK1 was more similar to blood NK cells than brain NK2, as evidenced by a higher Spearman correlation coefficient (Supplementary Fig. 10d). CellChat analysis showed two major secretory axes confined to NK cells and some T cell *Il18* and *Xcl1* signaling (Supplementary Fig. 10e–f). MdC4 was the main subset interacting with NK cells expressing *Il18r1* receptors, a known activator of NK cells[58], whereas clusters DC2 and DC9 interacted with NK cells through the *Xcl1–Xcr1* pathway, possibly indicating a role in cDC1 recruitment as previously reported[59].

Numbers and transcriptomes of brain-associated B cells were not changed by stroke (Supplementary Fig. 10g), suggesting a minor role of B cells during the acute and subacute phases of ischemic brain injury.

### Brain transcriptomic changes after stroke in aged mice

The inflammatory response to ischemic brain injury differs between young and aged mice both in the transcriptomic response and the cellular composition of brain-infiltrating immune cells[60]. Therefore, we explored whether aging alters cell signatures of immune cells and ECs after stroke by preparing single-cell transcriptomes from both male and female aged (17–20 months) Sham and D02 mice, and female aged D14 mice. Compared to young mice, aged mice had similar infarct sizes and cerebral blood flow (CBF) changes during occlusion and reperfusion. However, the mortality rate was much higher in aged males (Supplementary Fig. 14b,c). The cell clusters of young and aged brains showed largely overlapping positioning in the UMAP space, indicating the retention of the core transcriptome between the two groups (Fig. 6a,b). However, the frequency of infiltrating peripheral immune cell types differed between young and aged mice (Fig. 6c). Aged brains of Sham mice showed a higher frequency of T cells, whereas granulocytes and DCs were more prominent in Sham brains of young mice, indicating increased brain-associated T cells in the brains of aged mice as previously reported[61]. Overall, the cellular profile at D02 after stroke was comparable between groups, with a modest increase in neutrophils and decreased MdCs in aged mice as previously reported[60] (Fig. 6c). At D14, we observed increased T cells and reduced MdCs and DCs in aged compared to young mice. At the subclass level, we found that the distribution of microglia subclusters was similar between the age groups (Fig. 6d). MdC clusters MdC5 and MdC6 were reduced in aged brains, possibly reflecting the overall decreased brain MdC content at D14. Granulocytes showed a reduction in clusters Gran3 and Gran5 without overt changes in gene expression. T cells showed an expansion of CD8–NK T cells (Tc2) and
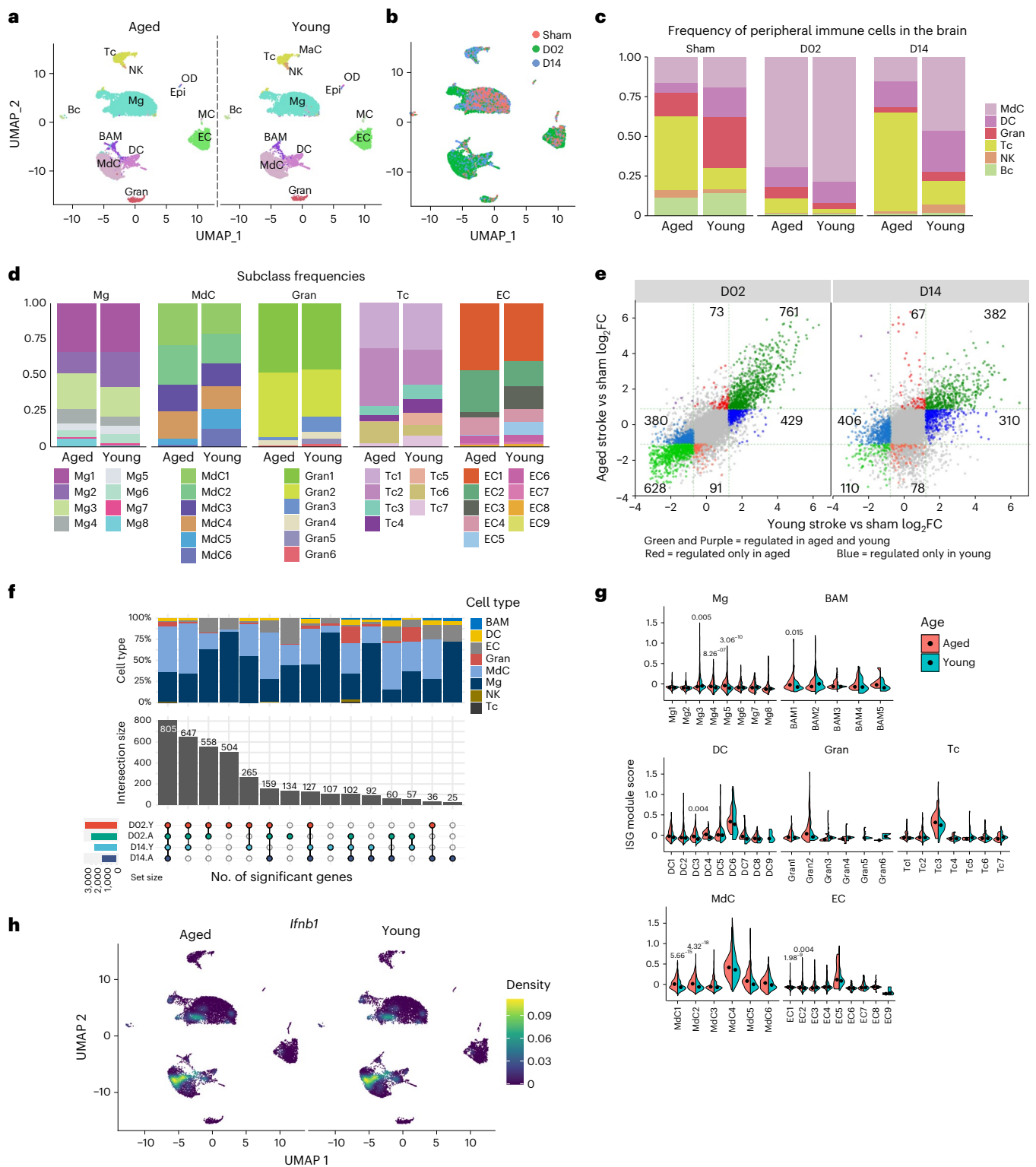
**Fig. 6 | Comparison of the cellular composition and transcriptome signatures of brain and blood cells in aged and young stroke mice. a**, UMAP plot representing color-coded brain cell clusters identified in aged and young single-cell transcriptomes. Tc, T cells; Bc, B cells; MC, vascular mural cells; Epi, epithelial-like cells; OD, oligodendrocytes. **b**, UMAP overlay of three color-coded time points of combined aged and young brain single-cell transcriptomes. **c**, Bar graph of relative frequencies of infiltrating peripheral immune cells in the brain across Sham, D02 and D14 groups. **d**, Bar graph showing relative frequencies of Mg, MdC, Gran, Tc and EC clusters in either aged or young stroke mice. **e**, Scatterplot comparing stroke-induced differential gene expression (DGE) versus Sham in young and aged mice at D02 and D14. Genes with $\log_2(FC)$ of >±1 and FDR < 0.05 are

highlighted in color. FC, fold change. The number of differentially regulated genes in each subgroup is indicated in the corresponding subquadrants. **f**, Lower panel: upset plot of DGE results showing overlapping and age-specific (A, aged; Y, young) DEGs in response to either acute (D02) or subacute (D14) stroke. Upper panel: bar graph indicating relative cell cluster contribution to the upset gene groups. **g**, Violin plots of ISG module scores in aged and young brain cell clusters. The dot shows the median value. Wilcoxon rank-sum test with Bonferroni correction was used to test for significance. $P$ values of <0.05 are plotted. Statistical details can be found in Source Data Fig. 6. **h**, Density plots in the UMAP space showing the expression of *Ifnb1* in the brain of young and aged mice. Scale bar represents densities based on kernel density estimation of gene expression.
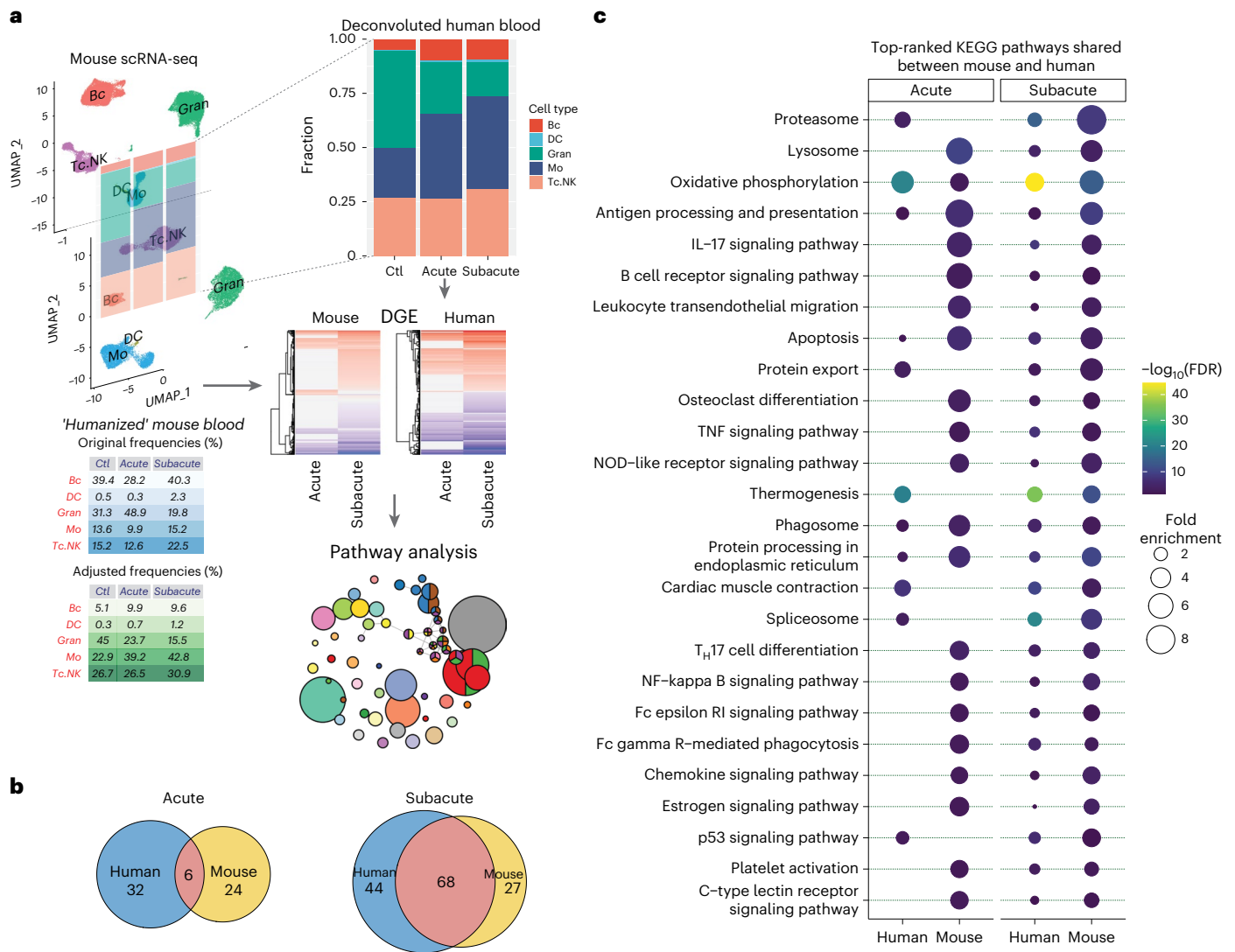
**Fig. 7 | Comparison of post-stroke transcriptomic profiles between mouse and human blood leukocytes by KEGG pathway analysis. a,** The analysis strategy included deconvolution of the human bulk-RNA-seq dataset (GSE122709), the 'humanizing' of the mouse blood to reflect the cellular composition in human stroke samples, determination of differential gene expression (DGE) and KEGG pathway analysis using pathfindeR. **b,** Euler diagrams showing distinct and shared enriched KEGG pathways (FDR < 0.05) between mouse and human peripheral blood leukocytes at acute and subacute time points after stroke. **c,** Top-ranked KEGG pathways that are shared between the human and mouse datasets. The color scale represents −log$_{10}$(FDR) and the point size depicts the enrichment score.

ILC2 (Tc6) clusters, whereas the frequency of γδT cells (Tc4) and T$_{reg}$ cells (Tc5) was reduced in aged brains[61]. Differential gene expression of all cell clusters between aged and young mice showed that the majority of genes were regulated in both aged and young mice, whereas the number of exclusively regulated genes was higher in young stroke mice than in aged mice (Fig. 6e). Young mice showed a higher number of regulated genes than aged mice, and acute stroke (D02) led to higher exclusively regulated genes than subacute stroke (D14) in both young and aged mice (Fig. 6f). In addition, most of the exclusive DEGs were detected in microglia, MdCs, ECs and to a lesser extend in granulocyte clusters (Fig. 6f). Among the specifically upregulated genes in aged mice were IFN-inducible genes, which was reflected by a higher ISG score in several microglia, MdC, DC and EC clusters in aged mice (Fig. 6g and Supplementary Fig. 11f). Although it has been suggested that IFNβ signaling attenuates post-ischemic inflammation[62], the cellular sources of type I IFNs in the post-ischemic brain have not been elucidated. In this study, we found that *Ifnb1* was upregulated in some MdCs and microglia clusters in both young and aged mice (Fig. 6h).

## The response to stroke in blood leukocytes: mouse versus human

To investigate whether transcriptional programs in peripheral blood leukocytes were conserved between mice and humans, we leveraged the data of a human RNA-seq study that was conducted at acute and subacute phases after ischemic stroke[63]. Given that humans and mice exhibit vastly different cellular composition in their blood leukocytes[64], we 'humanized' the mouse blood scRNA-seq dataset by readjusting the cellular composition to reflect that of the human dataset in controls and at acute and subacute phases after stroke as inferred by digital deconvolution (Fig. 7a). DEGs between controls, acute and subacute time points were determined in mouse and human datasets and mapped to Kyoto Encyclopedia of Genes and Genomes (KEGG) terms. For the acute time point, only 9% of identified pathways were shared among the human and mouse datasets. By contrast, 47% of pathways were shared at the subacute phase (Fig. 7b). Common pathways enriched in humans and mice were related to adaptive immunity (antigen processing and presentation, T$_H$17 cell differentiation, B cell receptor signaling), phagocytic

function and protein degradation (phagosome, Fc gamma R-mediated phagocytosis, C-type lectin receptor signaling, protein processing in endoplasmic reticulum, lysosome, proteasome), cytokine and inflammatory signaling (IL-17 signaling, TNF signaling, chemokine signaling, NOD-like receptor signaling, NF-κB signaling), altered apoptotic signaling (apoptosis, p53 signaling pathway) and oxidative phosphorylation (Fig. 7c and Supplementary Table 1). The molecular pathways selectively regulated in humans were largely related to altered cell metabolism involving sugars and amino acids (fructose, mannose, pyruvate and propanoate metabolism; glucagon signaling; valine, leucine and isoleucine catabolism) as well as pathways associated with cell proliferation (oocyte meiosis, pyrimidine metabolism) (Supplementary Fig. 12b). Pathways selectively regulated in mice included toll-like receptor signaling and neutrophil extracellular trap formation (Supplementary Fig. 12c). Taken together, the analysis shows higher similarities in the immune response to stroke in mice and humans during the subacute phase of stroke than in the acute phase.

## Discussion

We sought to investigate the cellular immune landscape in the brain after transient cerebral ischemia during the early and late phases of the injury, and relate cellular signatures found in the brain to the cellular states of blood immune cells. In addition, we compared the cellular response between young and aged mice and the response of blood leukocytes between mice and humans.

A major finding of this study is that there are distinct cellular transcriptomic responses of brain resident immune cells, infiltrating immune cells and ECs in the early and late phases of the tissue damage. Importantly, trajectory analysis showed that the transcriptome of blood-borne myeloid cells found in the brain after stroke remained distinct from their counterparts in the blood. These findings indicate that the local tissue milieu rather than peripheral immune priming determines the cellular state of MdCs and neutrophils (Supplementary Fig. 15).

Among the brain resident cells analyzed in this study, microglia showed the largest diversification in their transcriptional response across time points, whereas BAMs and ECs showed the strongest deviation from Sham states at D02 and the transcriptomes at D14 were more similar to the Sham condition. Microglia showed a strong proliferative response at D02, possibly triggered by the pronounced loss of microglia in the ischemic core. Similar proliferative responses have been observed after pharmacologic depletion of microglia[65], suggesting that depleting the microglial niche rather than a selective response to ischemic injury is inducing microglia proliferation. In addition to proliferative microglia, we identified another microglial subset with a phagocytic signature at D02, thus named 'clearing' microglia. Conversely, two main subsets denoting transcriptional states of inflammation were distinguished at D14, which resembled previously described signatures of DIM and DAM[16]. MdCs showed a continuous pseudotime trajectory originating from blood monocytes expressing *Ccr2* and *Ly6c2*, gradually losing monocytic marker genes and acquiring transcriptomic characteristics of tissue macrophages. This is consistent with a longitudinal in situ development of macrophage phenotypes that is independent of de novo recruitment of blood monocytes as previously suggested[66,67]. By contrast, and consistent with their short lifespan[68], brain granulocytes did not exhibit a pseudotime trajectory that was independent of their blood origins, resulting in trajectories that suggest continuous recruitment from the circulating pool. Limitations of this study include the restriction to two time points and the focus on immune cells and ECs; the response of other cell types including neurons and macroglia was not assessed.

Taken together, by analyzing the immune response in the brain and peripheral blood at single-cell resolution during acute and subacute stages after stroke, this study identifies cell type and time point specific immune programs and contributes to the ongoing efforts to compile a longitudinal cellular map of the immune response after stroke.

## Online content

Any methods, additional references, Nature Portfolio reporting summaries, source data, extended data, supplementary information, acknowledgements, peer review information; details of author contributions and competing interests; and statements of data and code availability are available at https://doi.org/10.1038/s41590-023-01711-x.

## References

1. Iadecola, C., Buckwalter, M. S. & Anrather, J. Immune responses to stroke: mechanisms, modulation, and therapeutic potential. *J. Clin. Invest.* **130**, 2777–2788 (2020).
2. Pedragosa, J. et al. CCR2 deficiency in monocytes impairs angiogenesis and functional recovery after ischemic stroke in mice. *J. Cereb. Blood Flow. Metab.* **40**, S98–S116 (2020).
3. Cuartero, M. I. et al. N2 neutrophils, novel players in brain inflammation after stroke: modulation by the PPARγ agonist rosiglitazone. *Stroke* **44**, 3498–3508 (2013).
4. Ito, M. et al. Brain regulatory T cells suppress astrogliosis and potentiate neurological recovery. *Nature* **565**, 246–250 (2019).
5. Qiu, M. et al. Cell heterogeneity uncovered by single-cell RNA sequencing offers potential therapeutic targets for ischemic stroke. *Aging Dis.* **13**, 1436–1454 (2022).
6. Beuker, C. et al. Stroke induces disease-specific myeloid cells in the brain parenchyma and pia. *Nat. Commun.* **13**, 945 (2022).
7. Zheng, J. et al. Single-cell RNA-seq analysis reveals compartment-specific heterogeneity and plasticity of microglia. *iScience* **24**, 102186 (2021).
8. Nakahashi-Oda, C. et al. CD300a blockade enhances efferocytosis by infiltrating myeloid cells and ameliorates neuronal deficit after ischemic stroke. *Sci. Immunol.* **6**, eabe7915 (2021).
9. Kim, S. et al. The antioxidant enzyme Peroxiredoxin-1 controls stroke-associated microglia against acute ischemic stroke. *Redox Biol.* **54**, 102347 (2022).
10. Li, X. et al. Single-cell transcriptomic analysis of the immune cell landscape in the aged mouse brain after ischemic stroke. *J. Neuroinflammation* **19**, 83 (2022).
11. Gelderblom, M. et al. Temporal and spatial dynamics of cerebral immune cell accumulation in stroke. *Stroke* **40**, 1849–1857 (2009).
12. Garcia-Bonilla, L., Iadecola, C. & Anrather, J. Cerebral ischemia and inflammation. In *Stroke 7th Edition Pathophysiology, Diagnosis, and Management* (Eds. Grotta, G. W. et al.) 117–128.e5 (Elsevier, 2021).
13. Matcovitch-Natan, O. et al. Microglia development follows a stepwise program to regulate brain homeostasis. *Science* **353**, aad8670 (2016).
14. Zheng, K. et al. Single-cell RNA-seq reveals the transcriptional landscape in ischemic stroke. *J. Cereb. Blood Flow. Metab.* **42**, 56–73 (2022).
15. Hammond, T. R. et al. Single-cell RNA sequencing of microglia throughout the mouse lifespan and in the injured brain reveals complex cell-state changes. *Immunity* **50**, 253–271.e6 (2019).
16. Keren-Shaul, H. et al. A unique microglia type associated with restricting development of Alzheimer's disease. *Cell* **169**, 1276–1290.e17 (2017).
17. Venkatraman, A. et al. Galectin-3: an emerging biomarker in stroke and cerebrovascular diseases. *Eur. J. Neurol.* **25**, 238–246 (2018).
18. Krasemann, S. et al. The TREM2-APOE pathway drives the transcriptional phenotype of dysfunctional microglia in neurodegenerative diseases. *Immunity* **47**, 566–581.e9 (2017).
19. Silvin, A. et al. Dual ontogeny of disease-associated microglia and disease inflammatory macrophages in aging and neurodegeneration. *Immunity* **55**, 1448–1465.e46 (2022).

20. Zanier, E. R., Fumagalli, S., Perego, C., Pischiutta, F. & De Simoni, M. G. Shape descriptors of the 'never resting' microglia in three different acute brain injury models in mice. *Intensive Care Med. Exp.* **3**, 7 (2015).

21. Masuda, T. et al. Specification of CNS macrophage subsets occurs postnatally in defined niches. *Nature* **604**, 740–748 (2022).

22. Viengkhou, B. & Hofer, M. J. Breaking down the cellular responses to type I interferon neurotoxicity in the brain. *Front Immunol.* **14**, 1110593 (2023).

23. Thored, P. et al. Long-term accumulation of microglia with proneurogenic phenotype concomitant with persistent neurogenesis in adult subventricular zone after stroke. *Glia* **57**, 835–849 (2009).

24. Van Hove, H. et al. A single-cell atlas of mouse brain macrophages reveals unique transcriptional identities shaped by ontogeny and tissue environment. *Nat. Neurosci.* **22**, 1021–1035 (2019).

25. Dani, N. et al. A cellular and spatial map of the choroid plexus across brain ventricles and ages. *Cell* **184**, 3056–3074.e21 (2021).

26. Miedema, A. et al. Brain macrophages acquire distinct transcriptomes in multiple sclerosis lesions and normal appearing white matter. *Acta Neuropathol. Commun.* **10**, 8 (2022).

27. Jaitin, D. A. et al. Lipid-associated macrophages control metabolic homeostasis in a Trem2-dependent manner. *Cell* **178**, 686–698. e14 (2019).

28. Yamaguchi, A. et al. Temporal expression profiling of DAMPs-related genes revealed the biphasic post-ischemic inflammation in the experimental stroke model. *Mol. Brain* **13**, 57 (2020).

29. Marcovecchio, P. M. et al. Scavenger receptor CD36 directs nonclassical monocyte patrolling along the endothelium during early atherogenesis. *Arterioscler Thromb. Vasc. Biol.* **37**, 2043–2052 (2017).

30. Amorim, A. et al. IFNγ and GM-CSF control complementary differentiation programs in the monocyte-to-phagocyte transition during neuroinflammation. *Nat. Immunol.* **23**, 217–228 (2022).

31. Cochain, C. et al. Single-cell RNA-seq reveals the transcriptional landscape and heterogeneity of aortic macrophages in murine atherosclerosis. *Circ. Res.* **122**, 1661–1674 (2018).

32. Williams, J. W. et al. Limited proliferation capacity of aortic intima resident macrophages requires monocyte recruitment for atherosclerotic plaque progression. *Nat. Immunol.* **21**, 1194–1204 (2020).

33. Rizzo, G. et al. Dynamics of monocyte-derived macrophage diversity in experimental myocardial infarction. *Cardiovasc. Res.* **119**, 772–785 (2023).

34. Gliem, M. et al. Macrophage-derived osteopontin induces reactive astrocyte polarization and promotes re-establishment of the blood brain barrier after ischemic stroke. *Glia* **63**, 2198–2207 (2015).

35. Nakano, Y. et al. Glycoprotein nonmetastatic melanoma protein B (GPNMB) as a novel neuroprotective factor in cerebral ischemia–reperfusion injury. *Neuroscience* **277**, 123–131 (2014).

36. Cai, W. et al. STAT6/Arg1 promotes microglia/macrophage efferocytosis and inflammation resolution in stroke mice. *JCI Insight* **4**, e131355 (2019).

37. Kalucka, J. et al. Single-cell transcriptome atlas of murine endothelial cells. *Cell* **180**, 764–779.e20 (2020).

38. Meng, H. et al. LRG1 promotes angiogenesis through upregulating the TGF-beta1 pathway in ischemic rat brain. *Mol. Med. Rep.* **14**, 5535–5543 (2016).

39. Minten, C. et al. DARC shuttles inflammatory chemokines across the blood–brain barrier during autoimmune central nervous system inflammation. *Brain* **137**, 1454–1469 (2014).

40. Wang, G. et al. Neutralization of lipocalin-2 diminishes stroke–reperfusion injury. *Int. J. Mol. Sci.* **21**, 6253 (2020).

41. Zhuang, X., Cross, D., Heath, V. L. & Bicknell, R. Shear stress, tip cells and regulators of endothelial migration. *Biochem. Soc. Trans.* **39**, 1571–1575 (2011).

42. Madureira, P. A. et al. The role of the annexin A2 heterotetramer in vascular fibrinolysis. *Blood* **118**, 4789–4797 (2011).

43. Hongu, T. et al. Perivascular tenascin C triggers sequential activation of macrophages and endothelial cells to generate a pro-metastatic vascular niche in the lungs. *Nat. Cancer* **3**, 486–504 (2022).

44. Rohlenova, K. et al. Single-cell RNA sequencing maps endothelial metabolic plasticity in pathological angiogenesis. *Cell Metab.* **31**, 862–877.e14 (2020).

45. Matsuoka, R. L., Buck, L. D., Vajrala, K. P., Quick, R. E. & Card, O. A. Historical and current perspectives on blood endothelial cell heterogeneity in the brain. *Cell. Mol. Life Sci.* **79**, 372 (2022).

46. Androvic, P. et al. Decoding the transcriptional response to ischemic stroke in young and aged mouse brain. *Cell Rep.* **31**, 107777 (2020).

47. Zhang, W. et al. Differential expression of receptors mediating receptor-mediated transcytosis (RMT) in brain microvessels, brain parenchyma and peripheral tissues of the mouse and the human. *Fluids Barriers CNS* **17**, 47 (2020).

48. Grieshaber-Bouyer, R. et al. The neutrotime transcriptional signature defines a single continuum of neutrophils across biological compartments. *Nat. Commun.* **12**, 2856 (2021).

49. Turk, V. et al. Cysteine cathepsins: from structure, function and regulation to new frontiers. *Biochim. Biophys. Acta* **1824**, 68–88 (2012).

50. Lee, H. K. et al. Neuroprotective and anti-inflammatory effects of a dodecamer peptide harboring Ninjurin 1 cell adhesion motif in the postischemic brain. *Mol. Neurobiol.* **55**, 6094–6111 (2018).

51. Evrard, M. et al. Developmental analysis of bone marrow neutrophils reveals populations specialized in expansion, trafficking, and effector functions. *Immunity* **48**, 364–379.e8 (2018).

52. Durai, V. et al. Cryptic activation of an *Irf8* enhancer governs cDC1 fate specification. *Nat. Immunol.* **20**, 1161–1173 (2019).

53. Xu, H. et al. Transcriptional atlas of intestinal immune cells reveals that neuropeptide α-CGRP modulates group 2 innate lymphoid cell responses. *Immunity* **51**, 696–708.e9 (2019).

54. Lee, J. Y. et al. The transcription factor KLF2 restrains CD4^{+} T follicular helper cell differentiation. *Immunity* **42**, 252–264 (2015).

55. Cai, W. Neuroprotection against ischemic stroke requires a specific class of early responder T cells in mice. *J Clin. Invest.* **132**, e157678 (2022).

56. Shichita, T. et al. Pivotal role of cerebral interleukin-17-producing γαT cells in the delayed phase of ischemic brain injury. *Nat. Med.* **15**, 946–950 (2009).

57. Miragaia, R. J. et al. Single-cell transcriptomics of regulatory T cells reveals trajectories of tissue adaptation. *Immunity* **50**, 493–504.e7 (2019).

58. Bjorkstrom, N. K., Strunz, B. & Ljunggren, H. G. Natural killer cells in antiviral immunity. *Nat. Rev. Immunol.* **22**, 112–123 (2022).

59. Bottcher, J. P. et al. NK cells stimulate recruitment of cDC1 into the tumor microenvironment promoting cancer immune control. *Cell* **172**, 1022–1037.e14 (2018).

60. Ritzel, R. M. et al. Aging alters the immunological response to ischemic stroke. *Acta Neuropathol.* **136**, 89–110 (2018).

61. Ritzel, R. M. et al. Age-associated resident memory CD8 T cells in the central nervous system are primed to potentiate inflammation after ischemic brain injury. *J. Immunol.* **196**, 3318–3330 (2016).

62. Inacio, A. R. et al. Endogenous IFN-β signaling exerts anti-inflammatory actions in experimentally induced focal cerebral ischemia. *J. Neuroinflammation* **12**, 211 (2015).

63. Han, R. et al. Differential expression and correlation analysis of global transcriptome for hemorrhagic transformation after acute ischemic stroke. *Front. Neurosci.* **16**, 889689 (2022).

64. Mestas, J. & Hughes, C. C. Of mice and not men: differences between mouse and human immunology. *J. Immunol.* **172**, 2731–2738 (2004).

65. Huang, Y. et al. Repopulated microglia are solely derived from the proliferation of residual microglia after acute depletion. *Nat. Neurosci.* **21**, 530–540 (2018).

66. Garcia-Bonilla, L. et al. Spatio-temporal profile, phenotypic diversity, and fate of recruited monocytes into the post-ischemic brain. *J. Neuroinflammation* **13**, 285 (2016).

67. Miro-Mur, F. et al. Immature monocytes recruited to the ischemic mouse brain differentiate into macrophages with features of alternative activation. *Brain Behav. Immun.* **53**, 18–33 (2016).

68. Hidalgo, A., Chilvers, E. R., Summers, C. & Koenderman, L. The neutrophil life cycle. *Trends Immunol.* **40**, 584–597 (2019).

# Methods

## Mice

All procedures were approved by the institutional animal care and use committee of Weill Cornell Medicine and were conducted in accordance with the ARRIVE guidelines[69,70]. Experiments were performed in young C57BL/6J (8–12 week old) male wild-type mice obtained from Jackson Laboratory (IMSR_JAX:000664; Bar Harbor, ME) and C57BL/6JN aged (17–18 month old) male and female wild-type mice obtained from the National Institute on Aging-National Institutes of Health (NIA-NIH). All in-house bred mice were also on a C57Bl/6J background and included B6.Cg-Gt(ROSA)26Sortm14(CAG-tdTomato)Hze/J (IMSR_JAX:007914) and B6.129P2(C)-Cx3cr1tm2.1(cre/ERT2)Jung/J (IMSR_JAX:020940). Mice were housed socially (three to five mice per cage) in individually ventilated cages, with ad libitum access to food and water and under controlled conditions (22 ± 2 °C, 12:12 h light:dark cycle with light phase from 07:00 to 19:00; 40–60% humidity).

## Middle cerebral artery occlusion

Transient focal cerebral ischemia was induced using the intraluminal filament model of middle cerebral artery (MCA) occlusion (MCAo) as previously described[71]. In brief, under isoflurane anesthesia (maintenance 1.5–2%), the MCA was occluded for 35 min using a 6-0 Doccol monofilament (no. L12; Sharon, MA). Reperfusion was confirmed by measuring the CBF in the MCA territory by transcranial laser Doppler flowmetry (Periflux System 5010, Perimed, King Park, NY). Only animals with CBF reduction of >85% during MCAo and CBF recovered by >80% after 10 min of reperfusion were included in the study[71]. Rectal temperature was monitored and kept constant (mean ± SE. 37.0 ± 0.5 °C) during the surgical procedure and in the recovery period until the animals regained full consciousness. After the procedure, mice were housed in a single chamber environmental incubator (Darwin Chambers, Saint Louis, MO) at 29–32 °C for up to 7 days. This system allows mice to maintain their body temperature post MCAo. Topical lidocaine and bupivacaine (0.25%, 0.1 ml, transdermal) were used for pre-operative analgesia, and buprenorphine (0.5 mg kg$^{-1}$ subcutaneously every 12 h) was used as post-operative analgesia for 72 h.

## Tamoxifen treatment

Four-week-old male Cx3cr1$^{CreER}$-tdTomato mice were treated with tamoxifen (T5648, Sigma; 80 mg kg$^{-1}$) dissolved in corn oil (C8267, Sigma) by intraperitoneal injection over five consecutive days. The mice were used for experiments 6–8 weeks after treatment.

## Cell isolation

Isolation of brain and blood cells from Sham and stroke mice was performed at the same time of the day (08:00–09:00) for all experiments to limit the effects of circadian gene expression variation[72]. Mice were anesthetized with pentobarbital (100 mg kg$^{-1}$, intraperitoneal) and transcardially perfused with heparinized PBS (2 U ml$^{-1}$). Cerebral right cortices were visually inspected after transcardial PBS perfusion to monitor for the presence of ischemic lesions. In brief, either control-sham or ischemic hemispheres were separated from the cerebellum and olfactory bulb and gently triturated using a Gentle MACS dissociator (Miltenyi Biotec, Auburn, CA). Single-cell suspensions were obtained by enzymatic digestion with papain (Neural Tissue Dissociation Kit (P), no. 130-092-628, Miltenyi Biotec) following the manufacturer's instructions. Four to five hemispheres were pooled for each experiment. In order to increase cell viability and to preserve the transcriptional state during the generation of single-cell suspensions, Brilliant Blue G (BBG, P2X7 receptor antagonist, 1 μM, Sigma), AP-5 (25 nM, NMDA receptor blocker, Tocris) and actinomycin D (RNA polymerase inhibitor, 5 μg ml$^{-1}$, Sigma) were added to the dissociation solution[73,74]. Next, the cell suspension was filtered through a 70 μm filter, resuspended in 30% Percoll (GE Healthcare)-HBSS containing 1 μM BBG, and spun for 10 min at 700×g. After gradient centrifugation,

the myelin layer was removed and the cell pellet was resuspended in 2% FBS–PBS buffer and filtered through a 40 μm filter. Isolated cells were washed and resuspended in 100 μl of blocking buffer per hemisphere to proceed to FACS staining and cell sorting.

For isolation of peripheral leukocytes, mice were anesthetized with pentobarbital (100 mg kg$^{-1}$, intraperitoneal) and 0.5 ml of blood was collected by cardiac puncture into heparinized tubes. For each experiment, the blood from two mice (1 ml total blood) was pooled and erythrocytes were lysed. BBG (1 μM) and actinomycin D (5 μg ml$^{-1}$) inhibitors were added during the isolation procedure. After erythrolysis, blood cells were resuspended in MACS buffer (PBS supplemented with 2% FBS, 2 mM EDTA; 300 μl per 10$^7$ cells) and incubated with a biotinylated Ter-119 antibody (Supplementary Table 2), and remaining erythrocytes were depleted with anti-biotin microbeads according to the manufacturer's instructions (Miltenyi Biotec). Afterward, cells were washed and resuspended in 0.01% BSA–PBS at a concentration of 10$^5$ leukocytes per ml for Drop-seq processing.

## Flow cytometry and cell sorting

For Drop-seq experiments, brain single-cell suspensions were incubated with anti-CD16/CD32 antibody for 10 min at 4 °C to block Fc receptors, followed by staining with CD45-BV510, Ly6C-FITC, CX3CR1-PE, Ly6G-PercP-Cy5.5 and CD11b-APC-Cy7 antibodies for 15 min at 4 °C (Supplementary Table 2). CD45$^{hi}$ cells, microglia (CD45$^{int}$CD11b$^+$CX3CR1$^+$) and ECs (CD45$^-$Ly6C$^+$) were sorted on an Aria II cytometer (BD Biosciences) and collected in 0.5 ml of 0.01% BSA–PBS for Drop-seq. Flow cytometry gating strategy is described in Supplementary Fig. 1a. Confirmation of brain damage was obtained after evaluating the infiltration of leukocytes in the ischemic brain (Supplementary Fig. 1b). Analytical flow cytometry was performed on a NovoCyte Flow Cytometer (Agilent, Santa Clara, CA). The antibodies used are described in Supplementary Table 2. Appropriate isotype controls, 'fluorescence minus one' staining, and staining of negative populations were used to establish gating parameters. Data were analyzed with FlowJo version 10.

## Generation of scRNA libraries by Drop-seq

Single-cell transcriptomes of sorted brain cells and purified blood leukocytes were prepared by Drop-seq as described[75] with modifications. Cells were resuspended in PBS–0.01% BSA to a final concentration of 100 cells per μl. Barcoded capture beads (ChemGenes Corporation, Wilmington, MA) were resuspended in 1.8 ml lysis buffer consisting of 4 M Guanidine HCL (ThermoFisher Scientific, Waltham, MA), 6% Ficoll PM-400 (Sigma-Aldrich), 0.2% Sarkosyl (Sigma-Aldrich, St. Louis, MO), 20 mM EDTA (ThermoFisher Scientific), 200 mM Tris pH 7.5 (Sigma-Aldrich), 50 mM DTT (Sigma-Aldrich) at a concentration of 120 beads per μl. A 5 mm diameter, 1.7 mm thick PVDF encapsulated magnetic stir disc and rotary magnetic tumble stirrer (V&P Scientific, San Diego, CA) was used along with a 3 ml syringe that contained the beads in lysis buffer to keep the beads in suspension. Thereafter, single cells and beads were encapsulated in nanoliter-scale droplets using a Drop-seq microfluidic device coated with Aquapel (FlowJEM, Toronto, Canada), droplet generation oil (BioRad, Hercules, CA) using flow rates of 4 ml h$^{-1}$ for cells and beads and 15 ml h$^{-1}$ for oil. Each run typically lasted about 18 min. After removing the oil, droplets were resuspended in 30 ml of 20–22 °C room temperature 6X SSC (Promega, Madison, WI) and 1 ml perfluorooctanol (Sigma-Aldrich, St. Louis, MO) and shaken vigorously six times vertically to break the droplets. The beads were captured by loading them into a 20 ml syringe with an attached 0.22 μm Millex-Gv syringe filter (Millipore Sigma, Burlington, MA) as previously described[76]. Beads were washed with 2 × 20 ml of ice-cold 6X SCC. The syringe filter was then inverted, and a 10 ml syringe was used to flush the beads out with 10 ml ice-cold 6X SSC repeated for a total of three times. Beads were collected by centrifugation at 1,250×g for 2 min at 4 °C with low brake setting. The remainder of the Drop-seq protocol

followed the published guidelines[75]. cDNA was amplified by PCR using the following parameters: 95 °C (3 min); four cycles of 98 °C (20 s), 65 °C (45 s), 72 °C (3 min); 11 cycles of 98 °C (20 s), 67 °C (20 s) and 72 °C (3 min). Libraries were quantified by quantitative PCR and checked for quality and size distribution on a Bioanalyzer (Agilent) before sequencing on an Illumina NextSeq500 instrument using the 75 cycle High Output v2 kit (Genomics Core Facility, Cornell University, Ithaca, NY). Three to four libraries were multiplexed into a single run. We loaded 1.8 pM library and provided Drop-seq Custom Read1 Primer at 0.3 µM in position seven of the reagent cartridge without PhiX spike-in using a read configuration of 20 bases (Read1), 8 bases (Index1) and 64 bases (Read2). Details regarding each Drop-seq run and characteristics of the strain, sex, age and number of mice used for transcriptomic analysis can be found in Supplementary Table 3.

### Data pre-processing
Demultiplexed fastq files were cleaned of reads that did not pass the Illumina Passing Filter with fastq_illumina_filter (version 0.1) and processed with the Drop-seq Tools (version 2.3.0) pipeline[77]. In brief, each transcriptome Read2 was tagged with the cell barcode (bases 1 to 12) and unique molecular identifier (UMI) barcode (bases 13 to 20) obtained from Read1, trimmed for sequencing adapters and poly-A sequences, and aligned to the mouse reference genome assembly (Ensembl GRCm38.94 release) using STAR (version 2.7.3a)[78]. Reads aligning to exons were tagged with the respective gene symbol, and counts of UMI-deduplicated reads per gene within each singular cell barcode were used to build a genes x cells count matrix. The matrix contained 40,000 cell barcodes associated with the highest numbers of UMIs. We used the DecontX method from the R package *celda* (version 1.12.0)[79], a Bayesian hierarchical model to estimate and remove cross-contamination from ambient RNA, to construct a corrected genes x cells count matrix. Cells with fewer than 200 UMIs, more than 10,000 UMIs or more than 20% mitochondrial genes were excluded. We used DoubletFinder (version 2.0.3)[80] to computationally detect cell doublets with an expected doublet rate of 5% (ref. 75) as an input parameter. Cells tagged with a 'Doublet' call were removed. Finally, the corrected count matrices were merged into a single matrix.

### Bioinformatic analysis and statistics
We used Seurat (version 4.1.0)[81] for downstream analysis using the following seven steps.

1. Counts were log-normalized for each cell using the natural logarithm of 1 + counts per ten thousand.
2. The 3,000 most variable genes were identified by calling *FindVariableFeatures*.
3. We next standardized expression values for each gene across all cells by Z-score transformation (*ScaleData*).
4. Principal component analysis (PCA) was performed on the scaled variable gene matrix. The R package harmony (version 0.1.1)[82] was used to correct the matrix for batch effects. The data from replicate experiments were combined into four sets so that each set included a Sham, D02 and D14 experiment. We ran harmony on the first 40 PCA dimensions with a maximum of 20 iterations.
5. We used UMAP[83] for dimensional reduction and visualization of harmony-derived embeddings in a two-dimensional space with preset parameters by invoking the *RunUMAP* function in Seurat, using the 40 first components of the harmony reduction.
6. We used the Louvain algorithm as implemented in *FindClusters* with a resolution setting of 1.2 for the brain and 0.7 for the peripheral blood dataset to perform graph-based clustering on the neighbor graph that was constructed with the *FindNeighbors* function call on harmony-derived embeddings.
7. After clustering, we used the model-based analysis of single-cell transcriptomics (MAST) algorithm (version 1.05)[84] in the *FindAllMarkers* function to find DEGs in each cluster based on the log-normalized expression matrix with parameters only. pos = T, min.pct = 0.1, logfc.threshold = log2(1.5), max.cells.per.ident = 2,000.

We performed unsupervised cell type annotation using the SingleR package (version 2.2.0)[85] with ImmGen[86], BrainImmuneAtlas[87] and Tabula Muris[88] as reference datasets (see Supplementary Fig. 2). Assignments were further manually validated by scoring the top ten DEGs for the presence of canonical marker genes for each cell type. On these bases, we assigned the metacells to microglia, BAMs, MdCs, granulocytes, mast cells, DCs, T cells, NK cells, B cells, ECs, vascular mural cells, epithelial-like cells, and oligodendrocyte clusters for the brain dataset, and monocytes, granulocytes, eosinophils–basophils, DCs, T cells, NK cells, B cells, various precursors and one unclassified cluster for the peripheral blood dataset.

To achieve further resolution of cell states, individual count matrices were generated based on the initial cluster designation, and steps 1–7 were repeated with the following modifications: mitochondrial, ribosomal and gene model (*Gm*) annotated genes were removed; step 2, 2,000 variable features were selected; step 4, harmony was run on the first 15 PCA dimensions; step 5, The 'min.dist' parameter in the *RunUMAP* function was set to 0.1 for clusters with more than 2,500 cells; step 6, *FindClusters* was performed at a resolution of 0.4. DEGs with a false discovery rate (FDR) < 0.05 were ranked by their $\log_2$(fold change), and z-scores were computed on the average gene expression across clusters for visualization in heatmaps.

### Cluster pruning and metacell exclusion
After subclustering, we detected several clusters within the brain dataset with high expression of microglial (*Hexb, Siglech, P2ry12*) marker genes together with either granulocyte (*S100a8, S100a9, Cxcr2*), DC (*Cd209a, Xcr1, Ccr7*), T cell (*Trac, Trbc2, Cd3d*), NK cell (*Nkg7, Gzma*) or macrophage (*Mrc1, Lyve1*) genes. Although we cannot exclude that this is caused by biological processes such as transcriptomic changes or engulfment of living cells by microglia as previously reported for neutrophils and lymphocytes[89], we opted to exclude these cells as potential cell doublets. Therefore, we manually removed 1,730 microglia, 287 DCs, 145 BAMs, 70 granulocytes, 65 T cells, and 41 NK metacells. After exclusion of these cells, we reran steps 1–7 on the main dataset and performed de novo subclustering as described above.

### Analysis of combined young and aged brain datasets
The dataset from aged (17–20 month) mice brains were preprocessed as described above. Cell identities in the aged mice brain dataset were assigned using the *FindTransferAnchors* and *TransferData* functions in Seurat using the young brain dataset as a reference. Seurat objects from young and aged mice were merged into a single object by retaining all cells of the aged brains and randomly down-sampling the young brain dataset. This resulted in balanced cell numbers among cell type classes in both datasets (Supplementary Table 4). Raw count data were processed as described above. The harmony algorithm was run on the first 40 principal components of the PCA. UMAP was computed on the first 40 harmony dimensions. Differential gene expression (Fig. 7e) was computed with limma-voom (version 3.50.0)[90] with default parameters after 'pseudobulk' conversion of individual experiments using the *aggregateAcrossCells* function of the *scuttle* R package (version 1.10.3)[91] following the removal of mitochondrial, ribosomal, hemoglobin, gene model (*Gm*) annotated genes, and the sex-specific genes (*Tsix, Xist*).

### Cell trajectory inference
We conducted the trajectory inference analysis using the dyno R package (version 0.1.2)[92]. Brain and peripheral blood datasets were merged

and randomly downsampled to a maximum of 1,000 cells per cluster and treatment. The merged dataset was subset to contain either microglia, blood monocytes and brain MdCs, or blood neutrophil and brain granulocyte clusters. The trajectory inference was performed on the 2,000 most variable genes selected with the Seurat *FindVariableFeatures* function. For granulocytes and for monocytes and MdCs, blood granulocytes and monocytes were designated as the starting population, respectively. For microglia, the starting population consisted of all microglia from Sham brains. The most appropriate trajectory inference method (Slingshot)[93] was selected based on dyno (*guidelines_shiny* function) recommendations. UMAP was calculated on the first 15 PCA dimensions and trajectories were visualized in a two-dimensional space by the *plot_dimred* function of the dyno package.

## CellChat analysis

Cell–cell interaction networks were constructed using the CellChat R package (version 1.6.1)[94] with a custom mouse ligand–receptor interaction database that contained combined entries of the curated RNAMagnet[95] and CellChat databases. In brief, the processed Seurat object was split by treatment into Sham, D02 and D14 datasets. Then, cell clusters were randomly downsampled to contain no more than 1,000 cells. The matrices were used as input for the *createCellChat* function and processed using its standard pipeline. Differentially expressed genes and interactions were identified in the CellChat object via *identifyOverExpressedGenes* and *identifyOverExpressedInteractions*, respectively. The CellChat algorithm was then run to calculate the probable interactions at the cell-to-cell level using *computeCommunProb* with 'truncatedMean' as the method for computing the average gene expression after removing 15% of observations from each end of the gene expression vector (parameter, trim = 0.15). The *filterCommunication* function was used to filter out interactions with less than 20 cells in each cluster. Communication probabilities on the signaling pathway level were then calculated by invoking the *computeCommunProbPathway* function. Ligand–receptor interaction probabilities were visualized by using *netVisual_aggregate* and *netVisual_individual*. For joint analysis of different group datasets (Sham, D02, D14), CellChat objects were merged, and *compareInteractions* was used to compare the total number and strength of interactions between treatments followed by the *rankNet* function for visualization.

## Modular score calculation and visualization

The *AddModuleScore* function in the Seurat package was used to calculate the functional signatures of each cell cluster. The type I interferon response score was calculated using ISGs as previously reported[96]. DAM and DIM scores were calculated using the gene list reported previously[19]. Additional module scores were calculated for foamy macrophages[32], stroke-associated macrophages[6] and monocytes[97]. All marker genes used for score calculation can be found in Supplementary Table 5. Module scores were visualized in R using the ggplot2 package (version 3.3.6)[98]. Data are expressed as median interquartile range (box plots).

## Correlation plots

Cluster-wise average gene expression was calculated with the *AverageExpression* function of the Seurat package. The *cor* function in R was used to construct a Spearman correlation matrix of gene expression between blood monocyte and brain MdC clusters. The correlation matrix was visualized with the *corrplot* function of the corrplot package (version 0.92)[99].

## Combined analysis of young and aged brain scRNA-seq data

Cell identities were assigned by aligning both datasets in the high-dimensional space and projecting cluster annotations from the young dataset onto the aged dataset essentially as previously described[81] and by using SingleR to adjudicate cell identities using the young dataset as a reference. For each cell, the maximal correlation score obtained by the two methods was used to assign the cell identity. The young dataset was downsampled to contain no more than 5,000 cells per treatment, and both datasets were merged and processed using steps 1–6 as outlined above ('Bioinformatic analysis and statistics'). Differential gene expression between aged and young mice was calculated for each cell cluster using the MAST algorithm of the *FindMarkers* function in Seurat with preset parameters after excluding mitochondrial, ribosomal, hemoglobin, sex-specific (*Tsix*, *Xist*) and gene model (*Gm*) annotated genes. Genes were considered differentially regulated if they showed higher than twofold change in expression level and an FDR < 0.05.

## Human–mouse comparison and pathway enrichment analysis

We searched the GEO database (query term: stroke[title] AND 'homo sapiens'[organism] AND 'expression profiling'; database status date: 05/28/2023), which identified six datasets that included peripheral blood mRNA analysis (GSE122709, GSE58294, GSE16561, GSE22255, GSE37587 and GSE199435). Only GSE122709 included acute and subacute time points after ischemic stroke and controls matched for age, sex and vascular risk factors including body mass index, hypertension and hyperlipidemia, and was therefore used for analysis[63]. We determined DEGs between control, acute (post-stroke day 1) and subacute (post-stroke day 7) samples using the quasi-likelihood $F$-test in edgeR (version 3.42.4)[100]. We performed active-subnetwork-oriented pathway enrichment analysis on DEGs with an FDR < 0.05 and an absolute fold change of >2 using the pathfindR package (version 2.3.0)[101] with Biogrid[102] as the protein interaction database and KEGG[103] as the pathway database, which was filtered to remove human disease terms. Next, we adjusted the mouse peripheral blood scRNA-seq dataset to match the cellular composition of human samples. The cellular composition was inferred after deconvoluting the gene count matrices included in GSE122709 using robust linear models as implemented in the ABIS web tool[104], which contains a signature expression matrix of 29 immune cell types obtained by RNA-seq of flow-sorted human peripheral blood leukocytes from 13 human donors. We adjusted the composition of T cells, NK cells, B cells, granulocytes, DCs and monocytes by experimental condition to match the average cellular composition of the human dataset in control, acute and subacute stroke patients. This compositionally adjusted dataset was processed for DEGs between conditions (Sham, D02, D14) using MAST as described above. DEGs with an FDR of <0.05 and an absolute fold change of >1.2 were used to query the KEGG database using pathfindeR. Significant KEGG terms (FDR < 0.05) from the human and mouse analysis were combined and visualized for overlapping terms using the eulerr package (version 7.0.0)[105]. For visualization of the top regulated KEGG terms, we pruned the list of KEGG terms by calculating a similarity matrix of terms by overlapping genes as implemented in the *term_similarity_from_KEGG* function of the simplifyEnrichment package (version 1.10.0)[106]. We used the obtained similarity matrix to cluster similar terms into term groups, invoking the *reduceSimMatrix* function of the rrvgo package (version 1.12.2)[107]. Terms were ranked by their enrichment score, and all terms with an enrichment score larger than the median enrichment score were selected for visualization. Results were visualized with the ggplot2 package. To validate our approach, we leveraged the data from the GEO GSE32529 dataset[108], which contains RNA array data of peripheral blood from mice undergoing MCAo 24 h before sample collection. Samples from naive mice (GSM805772–GSM805777) and 24 h stroke mice (GSM805853–GSM805856) were included in the analysis. Cell types were inferred using CibersortX[109] with the mouse-specific ImmuCC annotation matrix, which provides a matrix-weighted score to identify 25 different immune cell populations[110]. Adjustments of cellular composition, DGE and pathway enrichment analysis were conducted as described above for GSE122709.

## Brain histology

Mice were deeply anesthetized with sodium pentobarbital and transcardially perfused with ice-cold PBS (30 ml) followed by 4% paraformaldehyde in PBS (100 ml). Brains were dissected, post-fixed in 4% paraformaldehyde overnight, dehydrated in 30% PBS–sucrose solution for 1–2 days and then frozen using dry ice. Frozen brains were then embedded in Epredia M-1 Embedding Matrix (ThermoFisher Scientific) and cut in coronal sections using a cryostat (Leica CM3050S, Mannheim, Germany). The sections were mounted on slides for either IF downstream applications or RNA-FISH.

For IF, coronal 18 μm thick sections were permeabilized with 0.5% Triton X-100 (Sigma) in PBS (PBST), blocked with 5% normal donkey serum (NDS) in 0.1% PSBT for 1 h and incubated overnight at 4 °C with primary antibodies (Supplementary Table 2) in 1% NDS–0.1% PBST. After overnight incubation, sections were washed three times for 5 min with 0.1% PBST and incubated with secondary antibodies (Supplementary Table 2) in 1% NDS–0.1% PBST for 1 h at room temperature. Sections were washed with 0.1% PBST twice for 5 min, followed by a single 5 min wash in 0.1% PBST–DAPI (1:100, 12.5 ng μl$^{-1}$), mounted with FluorSave Reagent (Millipore) and visualized using either the Olympus IX83 or Leica TCS SP8 confocal microscopes.

RNA-FISH was performed using RNAscope Multiplex Fluorescent Kit v2 (ACD-Bio-Techne, Newark, CA) following the manufacturer's instructions. In brief, 10 μm thickness sections were processed using RNAscope hydrogen peroxide, followed by boiling Target Retrieval solution, dehydrated by 100% ethanol and incubated in Protease III solution. Then, tissue sections were hybridized with the target probes (Supplementary Table 2) for 2 h at 40 °C, followed by a series of signal amplification and washing steps. Hybridization signals were detected by fluorescent signal using peroxidase-based Tyramide Signal Amplification-Plus Fluorescein or TSA Plus Cyanine 5 (PerkinElmer, Shelton, CT). Finally, the sections were counterstained with DAPI and coverslipped using ProLong Gold Antifade Mountant. Images were acquired using either an epi-fluorescent (Olympus IX83, Waltham, MA) or a confocal (Leica) microscope. Images were analyzed using Fiji (version 2.14.0/1.54f)[111]. When FISH and IF staining were combined, the slides were washed in RNAscope wash buffer after the development of Tyramide Signal and then IF was sequentially performed as described above but skipping the permeabilization step.

## Measurement of infarct volume

As described in detail elsewhere[71], blinded assessment of infarct volume, corrected for swelling, was quantified 24–48 h after MCAo using Nissl stain on twelve 30 μm thick coronal brain sections and Fiji analysis software.

## Statistic and reproducibility

Experimental groups were defined by the number of elapsed days after surgery or/and by the genotype. No statistical methods were used to predetermine sample size; this was determined based on previous studies[66,112] or pilot experiments. For scRNA transcriptomic analysis, a total of $n = 83$ young male mice, $n = 4$ aged male mice and $n = 12$ aged female mice were used (Supplementary Table 5). Micrographs in Figs. 1f,i–m, 2f–i, 3j,l,m and 4f, Extended Data Figs. 2 and 3g and Supplementary Fig. 6c,d show representative examples from experiments performed in at least three mice that underwent either 2 days or 14 days of MCAo and one mouse that underwent Sham surgery. The non-lesioned hemisphere was also used as an internal control for the examined injured hemisphere. Each stain was repeated at least two times using serial brain coronal sections. Characteristics of the *Cx3cr1*-CreER$^{het}$Td$^{het}$ mice used for these IF experiments are provided in Supplementary Table 5 ($n = 9$ young male mice). Statistical analysis on infarct volume, changes in CBF and survival (Supplementary Fig. 14) was performed using GraphPad Prism (version 10). Statistical analysis of module scores (Fig. 6g) was conducted using rstatix (version 0.7.2)[113].

Statistical tests, $P$ values and sample sizes are indicated in figure panels and figure legends as appropriate. Differences were considered statistically significant at $P < 0.05$.

## Reporting summary

Further information on research design is available in the Nature Portfolio Reporting Summary linked to this article.

## Data availability

The raw and processed data and metadata of all scRNA-seq datasets included in this study are available in the GEO repository (GSE225948). A publicly accessible interactive web portal for exploring the scRNA-seq data included in this study has been developed (https://anratherlab. shinyapps.io/strokevis/). Source data are provided with this paper.

## Code availability

Code that supports the findings of this study are available from the corresponding author upon request.

## References

69. Kilkenny, C. et al. Animal research: reporting in vivo experiments— the ARRIVE guidelines. *J. Cereb. Blood Flow. Metab.* **31**, 991–993 (2011).
70. Percie du Sert, N. et al. The ARRIVE guidelines 2.0: updated guidelines for reporting animal research. *J. Physiol.* **598**, 3793–3801 (2020).
71. Jackman, K., Kunz, A. & Iadecola, C. Modeling focal cerebral ischemia in vivo. *Methods Mol. Biol.* **793**, 195–209 (2011).
72. Ximerakis, M. et al. Single-cell transcriptomic profiling of the aging mouse brain. *Nat. Neurosci.* **22**, 1696–1708 (2019).
73. Soltoff, S. P., McMillian, M. K. & Talamo, B. R. Coomassie Brilliant Blue G is a more potent antagonist of P$_2$ purinergic responses than Reactive Blue 2 (Cibacron Blue 3GA) in rat parotid acinar cells. *Biochem. Biophys. Res. Commun.* **165**, 1279–1285 (1989).
74. Hrvatin, S. et al. Single-cell analysis of experience-dependent transcriptomic states in the mouse visual cortex. *Nat. Neurosci.* **21**, 120–129 (2018).
75. Macosko, E. Z. et al. Highly parallel genome-wide expression profiling of individual cells using nanoliter droplets. *Cell* **161**, 1202–1214 (2015).
76. Datlinger, P. et al. Pooled CRISPR screening with single-cell transcriptome readout. *Nat. Methods* **14**, 297–301 (2017).
77. Saunders, A. et al. Molecular diversity and specializations among the cells of the adult mouse brain. *Cell* **174**, 1015–1030.e16 (2018).
78. Dobin, A. et al. STAR: ultrafast universal RNA-seq aligner. *Bioinformatics* **29**, 15–21 (2013).
79. Campbell, J., Yang, S., Wang, Z., Corbett, S. & Koga, Y. *celda: CEllular Latent Dirichlet Allocation* https://bioconductor.org/ packages/celda (2022).
80. McGinnis, C. S., Murrow, L. M. & Gartner, Z. J. DoubletFinder: doublet detection in single-cell RNA sequencing data using artificial nearest neighbors. *Cell Syst.* **8**, 329–337.e4 (2019).
81. Stuart, T. et al. Comprehensive integration of single-cell data. *Cell* **177**, 1888–1902.e21 (2019).
82. Korsunsky, I. et al. Fast, sensitive and accurate integration of single-cell data with Harmony. *Nat. Methods* **16**, 1289–1296 (2019).
83. Becht, E. et al. Dimensionality reduction for visualizing single-cell data using UMAP. *Nat. Biotechnol.* **37**, 38–44 (2019).
84. Finak, G. et al. MAST: a flexible statistical framework for assessing transcriptional changes and characterizing heterogeneity in single-cell RNA sequencing data. *Genome Biol.* **16**, 278 (2015).
85. Aran, D. et al. Reference-based analysis of lung single-cell sequencing reveals a transitional profibrotic macrophage. *Nat. Immunol.* **20**, 163–172 (2019).

86. Heng, T. S. et al. The Immunological Genome Project: networks of gene expression in immune cells. *Nat. Immunol.* **9**, 1091–1094 (2008).

87. Van Hove, H. et al. A single-cell atlas of mouse brain macrophages reveals unique transcriptional identities shaped by ontogeny and tissue environment. *Nat. Neurosci.* **13**, 206 (2019).

88. Tabula Muris, C. et al. Single-cell transcriptomics of 20 mouse organs creates a *Tabula Muris*. *Nature* **562**, 367–372 (2018).

89. Neumann, J. et al. Microglia cells protect neurons by direct engulfment of invading neutrophil granulocytes: a new mechanism of CNS immune privilege. *J. Neurosci.* **28**, 5965–5975 (2008).

90. Ritchie, M. E. et al. limma powers differential expression analyses for RNA-sequencing and microarray studies. *Nucleic Acids Res.* **43**, e47 (2015).

91. McCarthy, D. J., Campbell, K. R., Lun, A. T. & Wills, Q. F. Scater: pre-processing, quality control, normalization and visualization of single-cell RNA-seq data in R. *Bioinformatics* **33**, 1179–1186 (2017).

92. Saelens, W., Cannoodt, R., Todorov, H. & Saeys, Y. A comparison of single-cell trajectory inference methods. *Nat. Biotechnol.* **37**, 547–554 (2019).

93. Street, K. et al. Slingshot: cell lineage and pseudotime inference for single-cell transcriptomics. *BMC Genomics* **19**, 477 (2018).

94. Jin, S. et al. Inference and analysis of cell-cell communication using CellChat. *Nat. Commun.* **12**, 1088 (2021).

95. Baccin, C. et al. Combined single-cell and spatial transcriptomics reveal the molecular, cellular and spatial bone marrow niche organization. *Nat. Cell Biol.* **22**, 38–48 (2020).

96. Kim, H. et al. Development of a validated interferon score using NanoString technology. *J. Interferon Cytokine Res.* **38**, 171–185 (2018).

97. Ballesteros, I. et al. Co-option of neutrophil fates by tissue environments. *Cell* **183**, 1282–1297.e18 (2020).

98. Wickham, H. *ggplot2: elegant graphics for data analysis* (Springer-Verlag, 2016).

99. Wei, T. & Simko, V. *R package 'corrplot': visualization of a correlation matrix* https://github.com/taiyun/corrplot (2021).

100. Robinson, M. D., McCarthy, D. J. & Smyth, G. K. edgeR: a Bioconductor package for differential expression analysis of digital gene expression data. *Bioinformatics* **26**, 139–140 (2010).

101. Ulgen, E., Ozisik, O. & Sezerman, O. U. pathfindR: an R package for comprehensive identification of enriched pathways in omics data through active subnetworks. *Front. Genet.* **10**, 858 (2019).

102. Oughtred, R. et al. The BioGRID interaction database: 2019 update. *Nucleic Acids Res.* **47**, D529–D541 (2019).

103. Kanehisa, M. & Goto, S. KEGG: Kyoto Encyclopedia of Genes and Genomes. *Nucleic Acids Res.* **28**, 27–30 (2000).

104. Monaco, G. et al. RNA-Seq signatures normalized by mRNA abundance allow absolute deconvolution of human immune cell types. *Cell Rep.* **26**, 1627–1640.e27 (2019).

105. Larsson, J. & Gustafsson, P. A case study in fitting area-proportional Euler diagrams with ellipses using eulerr. In *CEUR Workshop Proceedings* (Eds. Sato, Y., & Shams, Z.) 84–91 (2018).

106. Gu, Z. & Hubschmann, D. simplifyEnrichment: a Bioconductor package for clustering and visualizing functional enrichment results. *Genomics Proteom. Bioinforma.* **21**, 190–202 (2023).

107. Sayols, S. *rrvgo: a Bioconductor package to reduce and visualize Gene Ontology terms* https://bioconductor.org/packages/release/bioc/html/rrvgo.html (2020).

108. Stevens, S. L. et al. Multiple preconditioning paradigms converge on interferon regulatory factor-dependent signaling to promote tolerance to ischemic brain injury. *J. Neurosci.* **31**, 8456–8463 (2011).

109. Newman, A. M. et al. Determining cell type abundance and expression from bulk tissues with digital cytometry. *Nat. Biotechnol.* **37**, 773–782 (2019).

110. Chen, Z. et al. Inference of immune cell composition on the expression profiles of mouse tissue. *Sci. Rep.* **7**, 40508 (2017).

111. Schindelin, J. et al. Fiji: an open-source platform for biological-image analysis. *Nat. Methods* **9**, 676–682 (2012).

112. Garcia-Bonilla, L. et al. Role of microglial and endothelial CD36 in post-ischemic inflammasome activation and interleukin-1β-induced endothelial activation. *Brain Behav. Immun.* **95**, 489–501 (2021).

113. Kassambara, A. *rstatix: pipe-friendly framework for basic statistical tests* https://CRAN.R-project.org/package=rstatix (2021).

## Acknowledgements

## Author contributions

J.A. and L.G.B. conceived the study with input from C.I. L.G.B., Z.S., R.S., O.N. and G.R. performed experiments and analyzed data. J.A. performed bioinformatic analyses. L.G.B. and J.A. wrote the original draft; C.I. revised the manuscript; all authors read and approved the final manuscript.

## Competing interests

C.I. serves on the scientific advisory board of Broadview Ventures. The other authors declare no competing interests.

## Additional information

**Extended data** is available for this paper at https://doi.org/10.1038/s41590-023-01711-x.

**Supplementary information** The online version contains supplementary material available at https://doi.org/10.1038/s41590-023-01711-x.

**Correspondence and requests for materials** should be addressed to Lidia Garcia-Bonilla or Josef Anrather.

**Peer review information** *Nature Immunology* thanks Louise McCullough and the other, anonymous, reviewer(s) for their contribution to the peer review of this work. S. Houston was the primary editor on this article and managed its editorial process and peer review in collaboration with the rest of the editorial team. Peer reviewer reports are available.

**Reprints and permissions information** is available at www.nature.com/reprints.
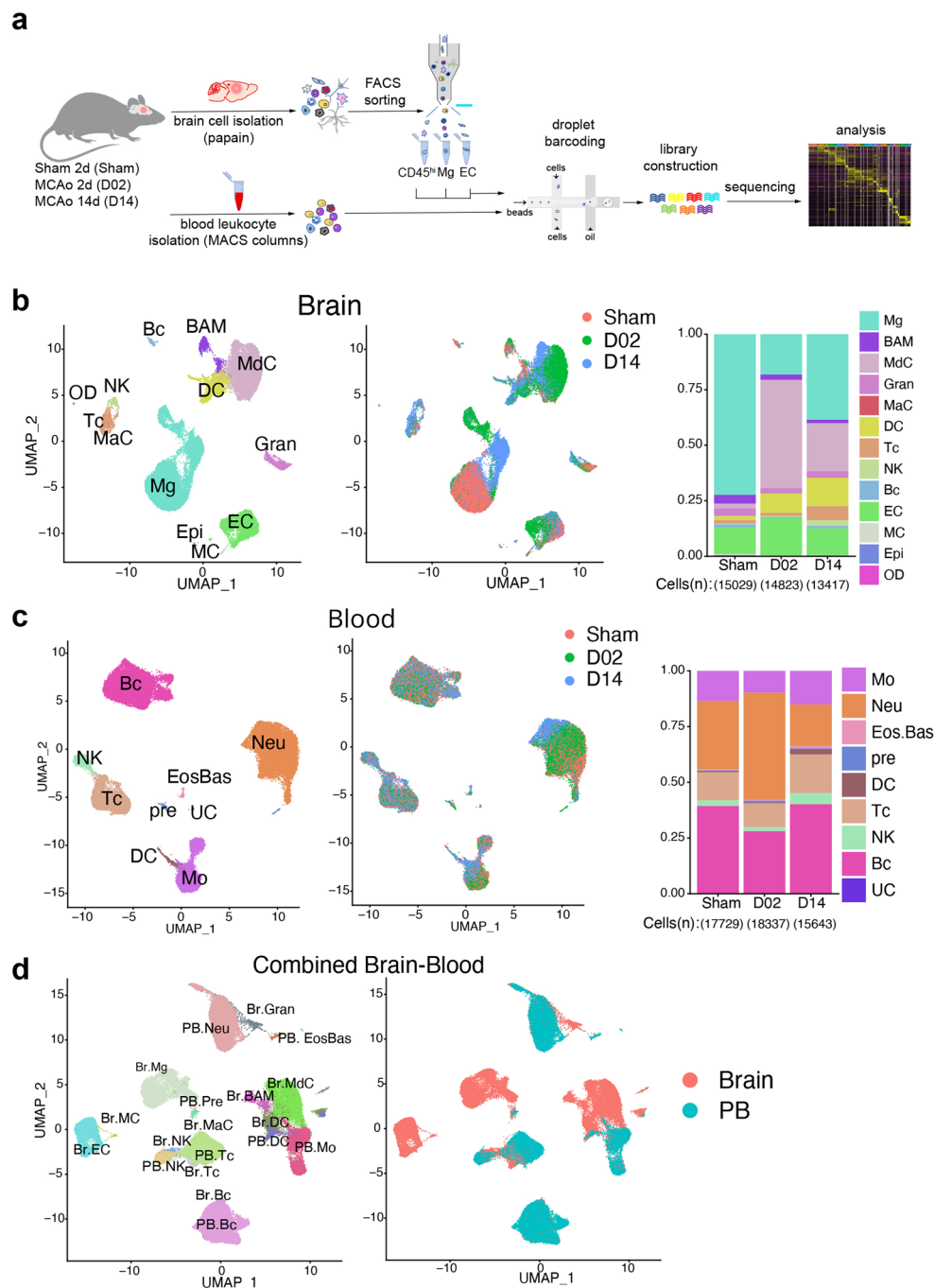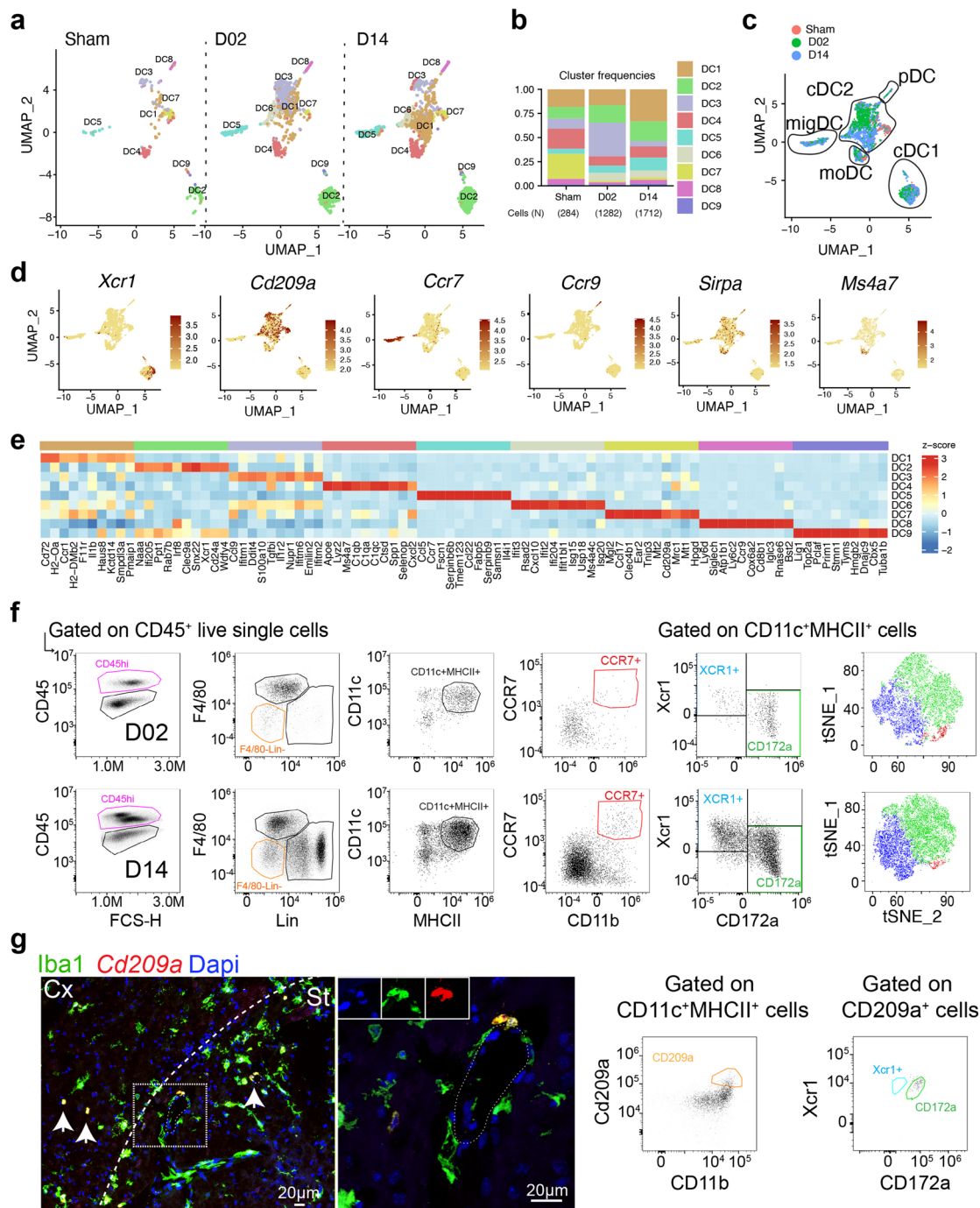
**Extended Data Fig. 1 | Single-cell transcriptomic profiling of mouse brain and blood cells after transient focal cerebral ischemia. a**, Schematic representation of Drop-Seq scRNA-seq pipeline used to analyze brain and blood cells isolated from either control surgery (Sham) or stroke mice 2 and 14 days (D02, D14) after injury. Brain cells were dissociated by enzymatic digestion with papain. Infiltrating leukocytes (CD45$^{hi}$), microglia (Mg) and endothelial cells (EC) were isolated by flow cytometry sorting. Blood leukocytes were purified after erythrocyte removal. Brain and blood single cell suspensions were subjected to Drop-Seq, sequencing and analysis. **b**, **c**, *Left*: UMAP plot representing color-coded cell clusters identified in merged brain (**b**) or blood (**c**) single-cell transcriptomes; *Middle*: UMAP of 3 color-coded time point overlay of brain

(**b**) or blood (**c**) single-cell transcriptomes; *Right*: bar graph showing relative frequencies of each cell type across Sham, D02 and D14 groups of either brain (**b**) or blood (**c**) identified cell type clusters. **d**, *Left*: UMAP plot of the combined brain (Br) and blood (PB) dataset showing cell clustering similarities between brain and blood Gran, Tc, Bc and brain myeloid cells (BAM, MdC, DC) with blood monocytes (left). *Right*: Same UMAP plot annotated by tissue. Border-associated macrophages (BAM), monocyte-derived cells (MdC), granulocytes (Gran), mast cells (MaC), dendritic cells (DC), T cells (Tc), NK cells (NK), B cells (Bc), vascular mural cells (MC), epithelial-like cells (Epi), oligodendrocytes (OD); Eosinophils-Basophils (EosBas); Monocytes (Mo); hematopoietic precursors (pre); unclassified (UC).
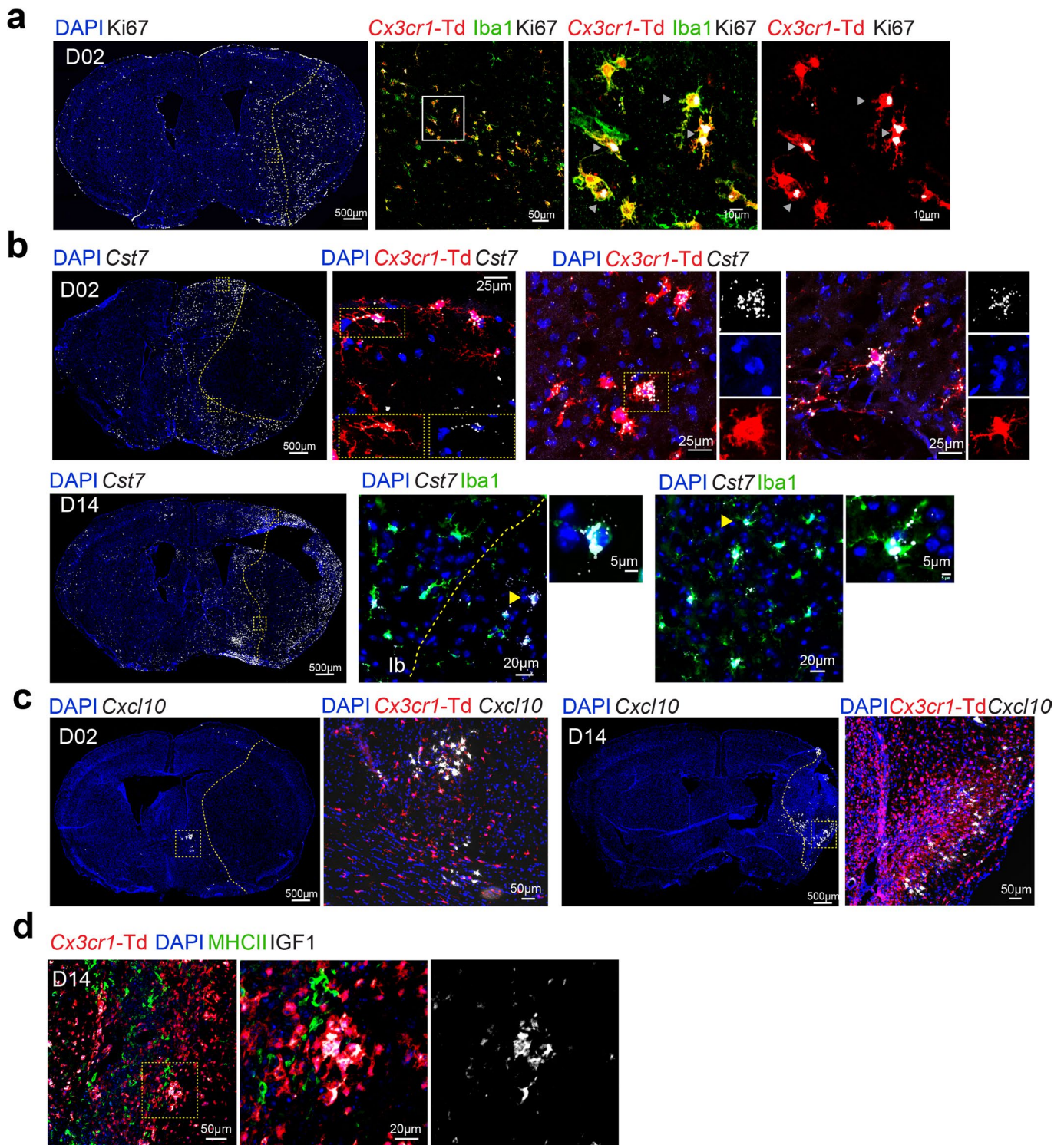
**Extended Data Fig. 2 | Histological validation of microglia marker genes (related to Fig. 1). a**, *left*: Representative immunofluorescence (IF) image of a whole brain section from a *Cx3cr1*^CreERT2^:R26Tdomato mouse subjected to 2 days of MCAo (D02) showing the distribution of Ki67⁺ cells (white, binary mask) and nuclear DAPI staining (blue); *middle and right panels*: IF images of magnified areas showing Ki67 expression by Td⁺(red) Iba1⁺(green) microglia in the peri-infarct area. Arrowheads indicate Ki67 staining. The border of the ischemic lesion is indicated by yellow dash outline and was traced based on DAPI, Iba1 and Tomato labels. **b**, *top*: RNAscope fluorescence in situ hybridization (FISH) validating *Cst7* (white) expression in D02 Td⁺ microglia (red). *Left*: Representative whole brain section image of *Cst7* expression (binary mask) and nuclear DAPI staining; *Middle and right panels:* FISH-IF images of magnified areas showing upregulation of *Cst7* in microglial cells surrounding the ischemic lesion.

*Bottom*: FISH-IF images validating *Cst7* (white) expression in D14 mice. *Left*: Representative whole brain section image of *Cst7* expression (binary mask) and nuclear DAPI staining; *Middle and right top panels:* FISH-IF images of magnified areas showing upregulation of *Cst7* in microglia (Iba1⁺, green) surrounding the ischemic lesion. **c**, FISH-IF images validating *Cxcl10* (white) expression in *Cx3cr1*-Td⁺ mice 2 and 14 days after MCAo. *Left* (D02): Representative whole brain section image of *Cxcl10* expression (binary mask) and images of magnified areas showing localization of *Cxcl10* in microglial cells (Td⁺, red) outside of the ischemic lesion. *Right* (D14): Representative whole brain section image of *Cxcl10* expression (binary mask) and images of magnified areas showing localization of *Cxcl10* in microglial cells (Td⁺, red) on the border of the ischemic lesion. **d**, IF images validating IGF1 (white) expression by *Cx3cr1*-Td⁺(red) MHCII⁻ (green) microglia 14 days after MCAo in the ischemic region.

**Extended Data Fig. 3 | Cellular composition and transcriptomics of brain dendritic cells. a**, UMAP plots of brain dendritic cells (DC) transcriptomes for each studied time point identifies 9 clusters (DC1-9). **b**, Bar graph showing relative frequencies of DC clusters across Sham, D02 and D14 groups. **c**, UMAP of 3 color-coded time point overlay of brain DC. Classification of clusters into DC subtypes is based on marker gene expression (d,f): cDC1 (*Xcr1, Clec9a*), cDC2 (*Cd209a, Sirpa*), monocyte derived-DC (moDC; *Sirpa, Ms4a7*), migratory (migDC; *Ccr7*), and plasmacytoid DC (pDC; *Ly6d, Ccr9*). **d**, UMAP plots displaying expression of marker genes for each identified DC cluster in the brain. Scale bars represent log of normalized gene expression. **e**, Heatmap displaying differential expression of the top 10 upregulated genes in each DC cluster. Scale bar represents Z-score of average gene expression (log). **f**, Flow cytometry analysis validating brain cDC1 (XCR1^{+}), cDC2 (CD172a^{+}) and migDC (CCR7^{+}) subtypes identified by scRNA-seq after stroke. **g**, *Left:* FISH of *Cd209a* (red) expression in the brain, combined with IF for Iba1 (green) and nuclear staining with DAPI (blue), showing *Cd209a*^{+}Iba1^{+} cells around blood vessel (dotted line). Cx: cortex; St: striatum. *Right*: Flow cytometry analysis showing double positive CD209a^{+}CD172a^{+} DC (CD11c^{+}MHCII^{+}).
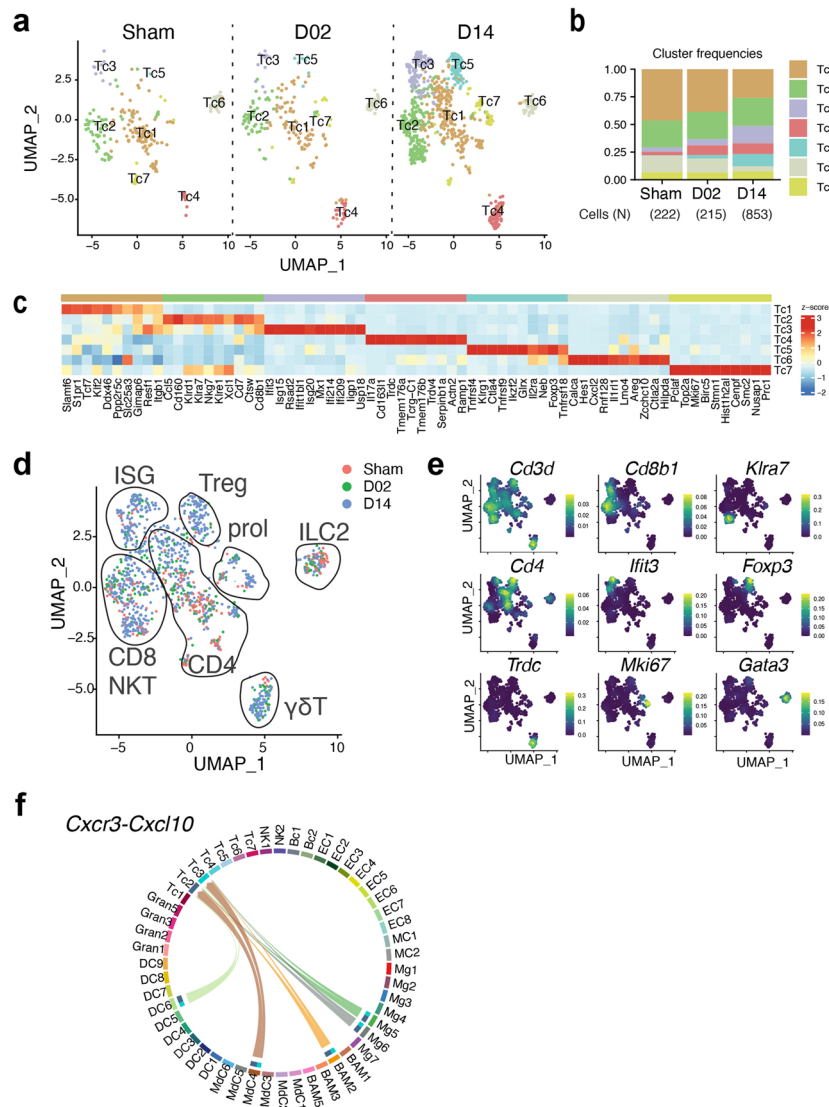
**Extended Data Fig. 4 | Cellular composition and transcriptomics of brain lymphoid cells. a**, UMAP plots of brain lymphoid cells (Tc) transcriptomes for each studied time point identifies 7 clusters (Tc1-7). **b**, Bar graph showing relative frequencies of Tc clusters across Sham, D02 and D14 groups. **c**, Heatmap displaying expression of the top 10 upregulated genes in each Tc cluster. Scale bar represents Z-score of average gene expression (log). **d**, UMAP of merged Sham, D02 and D14 Tc transcriptomes. Classification of clusters into T cell types is based on marker gene expression (c,e): CD4 (*Cd3d,Cd4*), Treg (*Cd3d,Cd4,Foxp3*), CD8 (*Cd3d, CD8b1*), NKT (*Cd3d, Gzma*), γδT (*Cd3d, Trdc*), interferon stimulated T cells (ISG; *Cd3d, Ifit3*), innate lymphoid cells type 2 (ILC2;

*Gata3, Hes1*) and proliferating T cells (prol; *Cd3d, Top2a*). **e**, Density plots in the UMAP space showing the expression of selected marker genes used for lymphoid cell type identification. Scale bars represent densities based on kernel density estimation of gene expression using. **f**, Chord plot showing cell-cell interactions between *Cxcr3* and *Cxcl10* in grouped Sham, D02 and D14 stroke mice. The strength of the interaction is indicated by the edge thickness. The color of the chord matches the cell cluster color sending the signal (*Cxcl10*). The number of cell recipient clusters (*Cxcr3*) and their weight in the interactions is indicated by the color-matched stacked bar next to each sender.

# nature portfolio

Corresponding author(s): Josef Anrather, Lidia Garcia-Bonilla

Last updated by author(s): Sep 8, 2023

# Reporting Summary

Nature Portfolio wishes to improve the reproducibility of the work that we publish. This form provides structure for consistency and transparency in reporting. For further information on Nature Portfolio policies, see our Editorial Policies and the Editorial Policy Checklist.

## Statistics

For all statistical analyses, confirm that the following items are present in the figure legend, table legend, main text, or Methods section.

| n/a | Confirmed | |
|---|---|---|
| ☐ | ☒ | The exact sample size (*n*) for each experimental group/condition, given as a discrete number and unit of measurement |
| ☐ | ☒ | A statement on whether measurements were taken from distinct samples or whether the same sample was measured repeatedly |
| ☐ | ☒ | The statistical test(s) used AND whether they are one- or two-sided<br>*Only common tests should be described solely by name; describe more complex techniques in the Methods section.* |
| ☐ | ☒ | A description of all covariates tested |
| ☐ | ☒ | A description of any assumptions or corrections, such as tests of normality and adjustment for multiple comparisons |
| ☐ | ☒ | A full description of the statistical parameters including central tendency (e.g. means) or other basic estimates (e.g. regression coefficient) AND variation (e.g. standard deviation) or associated estimates of uncertainty (e.g. confidence intervals) |
| ☐ | ☒ | For null hypothesis testing, the test statistic (e.g. *F*, *t*, *r*) with confidence intervals, effect sizes, degrees of freedom and *P* value noted<br>*Give P values as exact values whenever suitable.* |
| ☒ | ☐ | For Bayesian analysis, information on the choice of priors and Markov chain Monte Carlo settings |
| ☒ | ☐ | For hierarchical and complex designs, identification of the appropriate level for tests and full reporting of outcomes |
| ☒ | ☐ | Estimates of effect sizes (e.g. Cohen's *d*, Pearson's *r*), indicating how they were calculated |

*Our web collection on statistics for biologists contains articles on many of the points above.*

## Software and code

Policy information about availability of computer code

| Data collection | Periflux System 5010, Perimed, King Park, NY, was used for CBF measurement. Flow cytometry data were collected by NovoCyte Flow Cytometer (Agilent, Santa Clara, CA) and Aria II cytometer (BD Bioscience). Immunofluorescence images were acquired by epifluorescent microscopy (IX83 Inverted Microscope, Olympus, Center Valley, PA) or by confocal microscopy (Leica TCS SP8, Buffalo Grove, IL). Drop-seq microfluidic device (FlowJEM, Toronto Canada) and Illumina NextSeq500 were used for scRNAseq. |
|---|---|
| Data analysis | ABIS (https://github.com/giannimonaco/ABIS)<br>corrplot (Vers. 0.92; RRID:SCR_023081)<br>CibersortX (https://cibersortx.stanford.edu)<br>GraphPad Prism (Vers. 10; RRID:SCR_002798)<br>Periflux System 5010, Perimed,K ing Park,NY<br>harmony (Vers. 0.1.1; RRID:SCR_022206)<br>dyno (Vers. 0.1.2; https://github.com/dynverse/dyno)<br>simplifyEnrichment (Vers. 1.10.0; https://github.com/jokergoo/simplifyEnrichment)<br>celda (Vers. 1.12.0; https://github.com/campbio/celda)<br>SingleR (Vers. 2.2.0; RRID:SCR_023120)<br>Drop-seq Tools (Vers. 2.3.0; RRID:SCR_018142)<br>pathfindR (Vers. 2.3.0; https://github.com/egeulgen/pathfindR)<br>Fiji (Vers. 2.14.0/1.54f; RRID:SCR_002285).<br>Seurat (Vers. 4.1.0; RRID:SCR_016341)<br>rstatix (Vers. 0.7.2; RRID:SCR_021240) |

CellChat (Vers. 1.6.1; RRID:SCR_021946)
FlowJo (Vers. 10.8.1; RRID:SCR_008520)
rrvgo (Vers. 1.12.2; https://github.com/ssayols/rrvgo)
ComplexUpset (Vers. 1.3.3; RRID:SCR_022752)
scuttle (Vers. 1.10.3; https://github.com/LTLA/scuttle)
STAR (Vers. 2.7.3a; RRID:SCR_004463)
NovoExpress (Vers. 1.5.6; https://www.agilent.com/en/product/research-flow-cytometry/flow-cytometry-software/novocyte-novoexpress-software-1320805)
ggplot2 (Vers. 3.3.6; RRID:SCR_014601)
MAST (Vers. 1.05; RRID:SCR_016340)
DoubletFinder (Vers. 2.0.3; RRID:SCR_018771)
edgeR (Vers. 3.42.4; RRID:SCR_012802)
limma (Vers. 3.50.0; RRID:SCR_010943)
eulerr package (Vers. 7.0.0; RRID:SCR_022753)

Code that supports the findings of this study are available from the corresponding author upon request.

For manuscripts utilizing custom algorithms or software that are central to the research but not yet described in published literature, software must be made available to editors and reviewers. We strongly encourage code deposition in a community repository (e.g. GitHub). See the Nature Portfolio guidelines for submitting code & software for further information.

# Data

Policy information about availability of data

All manuscripts must include a data availability statement. This statement should provide the following information, where applicable:
- Accession codes, unique identifiers, or web links for publicly available datasets
- A description of any restrictions on data availability
- For clinical datasets or third party data, please ensure that the statement adheres to our policy

The raw and processed data and metadata of all scRNA-seq datasets included in this study are available in the GEO repository (GSE225948). A public accessible interactive web portal for exploring the scRNA-seq data included in this study has been developed (https://anratherlab.shinyapps.io/strokevis/). Ensembl GRCm38.94 database and GSE122709 and GSE32529 datasets have been used for this study.

# Research involving human participants, their data, or biological material

Policy information about studies with human participants or human data. See also policy information about sex, gender (identity/presentation), and sexual orientation and race, ethnicity and racism.

| | |
|---|---|
| Reporting on sex and gender | N/A |
| Reporting on race, ethnicity, or other socially relevant groupings | N/A |
| Population characteristics | N/A |
| Recruitment | N/A |
| Ethics oversight | N/A |

Note that full information on the approval of the study protocol must also be provided in the manuscript.

# Field-specific reporting

Please select the one below that is the best fit for your research. If you are not sure, read the appropriate sections before making your selection.

☒ Life sciences          ☐ Behavioural & social sciences          ☐ Ecological, evolutionary & environmental sciences

For a reference copy of the document with all sections, see nature.com/documents/nr-reporting-summary-flat.pdf

# Life sciences study design

All studies must disclose on these points even when the disclosure is negative.

| | |
|---|---|
| Sample size | Sample size was determined according to power analysis based on previous works published by our lab on mouse stroke models. Based on the anticipated differences and data variance, n= 8 are required to achieve a power of 0.85-0.9 in experiments involving stroke volume measurement.<br>Garcia-Bonilla, L. et al. Endogenous Protection from Ischemic Brain Injury by Preconditioned Monocytes. J Neurosci 38, 6722-6736 (2018). https://doi.org/10.1523/JNEUROSCI.0324-18.2018<br>2 Garcia-Bonilla, L., Racchumi, G., Murphy, M., Anrather, J. & Iadecola, C. Endothelial CD36 Contributes to Postischemic Brain Injury by Promoting Neutrophil Activation via CSF3. J Neurosci 35, 14783-14793 (2015). https://doi.org/10.1523/JNEUROSCI.2980-15.2015 |

3 Garcia-Bonilla, L. et al. Inducible nitric oxide synthase in neutrophils and endothelium contributes to ischemic brain injury in mice. J Immunol 193, 2531-2537 (2014). https://doi.org:10.4049/jimmunol.1400918
4 Jackman, K. et al. Progranulin deficiency promotes post-ischemic blood-brain barrier disruption. J Neurosci 33, 19579-19589 (2013). https://doi.org:10.1523/JNEUROSCI.4318-13.2013
5 Garcia-Bonilla, L. et al. Role of microglial and endothelial CD36 in post-ischemic inflammasome activation and interleukin-1beta-induced endothelial activation. Brain Behav Immun 95, 489-501 (2021). https://doi.org:10.1016/j.bbi.2021.04.010
6 Garcia-Bonilla, L. et al. Spatio-temporal profile, phenotypic diversity, and fate of recruited monocytes into the post-ischemic brain. J Neuroinflammation 13, 285 (2016). https://doi.org:10.1186/s12974-016-0750-0
7 Benakis, C. et al. Commensal microbiota affects ischemic stroke outcome by regulating intestinal gammadelta T cells. Nat Med 22, 516-523 (2016). https://doi.org:10.1038/nm.4068

| | |
|---|---|
| Data exclusions | One Drop-seq experiment from peripheral blood leukocytes was excluded because library preparation failed for this sample. |
| Replication | Biological and technical replicates are indicated in Supplementary Table 3. |
| Randomization | Mice within cages were randomly allocated to Sham, D02 or D14 groups reducing possible biases. |
| Blinding | For the Drop-seq experiments, investigators were not blinded to group allocation during data collection because experimental groups were easily discernible since they were determined by time after stroke and mouse age and sex. The computational analysis pipeline was identical for all processed samples, and intended to be unbiased, so blinding was not relevant for transcriptomic analysis. Data collection, sample processing, and data analysis of infarct volume was performed in a blinded fashion. |

# Reporting for specific materials, systems and methods

We require information from authors about some types of materials, experimental systems and methods used in many studies. Here, indicate whether each material, system or method listed is relevant to your study. If you are not sure if a list item applies to your research, read the appropriate section before selecting a response.

## Materials & experimental systems

| n/a | Involved in the study |
|---|---|
| ☐ | ☒ Antibodies |
| ☒ | ☐ Eukaryotic cell lines |
| ☒ | ☐ Palaeontology and archaeology |
| ☐ | ☒ Animals and other organisms |
| ☒ | ☐ Clinical data |
| ☒ | ☐ Dual use research of concern |
| ☒ | ☐ Plants |

## Methods

| n/a | Involved in the study |
|---|---|
| ☒ | ☐ ChIP-seq |
| ☐ | ☒ Flow cytometry |
| ☒ | ☐ MRI-based neuroimaging |

## Antibodies

| | |
|---|---|
| Antibodies used | CD11b APC/Cy7 M1/70 rat IgG2b, κ Biolegend AB_830641
CD11c PE/Cy7 N418 Armenian hamster Biolegend AB_493569
CD16/CD32  93 rat IgG2b, λ Biolegend AB_312800
CD172a AF700 P89 Rat IgG1, κ Biolegend AB_2650812
CD4 F488 RM4-5 rat IgG2a, κ Biolegend AB_493373
CD45  BV510 30F-11 rat IgG2b, κ Biolegend AB_2561392
CD45  APC 30F-11 rat IgG2b, κ Biolegend AB_312976
CX3CR1 PE SA011F11 rat IgG2a, κ Biolegend AB_2564314
F4/80 PE-Cy5 BM8 rat IgG2a, κ Biolegend AB_893494
I-A/I-E BV605 M5/114.15.2 rat IgG2b, κ  Biolegend AB_2565894
Ly6C FITC HK1.4 rat IgG2c, κ Biolegend AB_1186134
Ly6G PerCP/Cy5.5 1A8 rat IgG2a, κ Biolegend AB_1877272
Ly6G APC 1A8 rat IgG2a, κ Biolegend AB_1877163
TCR β PerCP/Cy5.5 H57-597 Armenian hamster Biolegend AB_1575176
TER-119 Biotin TER-119 rat IgG2b, κ Biolegend AB_313704
XCR1 PerCP/Cy5.5 ZET mouse IgG2b, κ Biolegend AB_2564363
CD197 (CCR7) PE 4B12 rat IgG2a, κ Biolegend AB_2564363
CD209a PE MMD3 mouse IgG2c, κ Biolegend AB_2721636
CD19 FITC 6D5 rat IgG2a, κ Biolegend AB_313640
CD3ε FITC 145-2C11 Armenian hamster Biolegend AB_312670
Ly6G FITC 1A8 rat IgG2a, κ Biolegend AB_1236488
NK1.1 FITC PK136 mouse IgG2a, κ Biolegend AB_313392
TCR β FITC H57-597 Armenian hamster Biolegend AB_313428
IGF1 mouse Sm1.2 IgG1k Millipore 05-172 AB_309643
CD206 rat MR5D3 IgG2a BioRad MCA2235 AB_324622
Iba1 rabbit polyclonal  Wako 019-19741 AB_839504
DsRed (TdTomato) rabbit polyclonal  Takara 632496 AB_10013483 |

Anti-MHC II (I-a/I-E) rat M5/114 IgG2bk Millipore MABF33 AB_10807702
Rat anti Mouse F4/80-biotin rat BM8 IgG2a Biolegend 123105 AB_893499
Fluorescein (FITC) AffiniPure Donkey Anti-Mouse IgG (H+L) donkey polyclonal  Jackson ImmunoResearch Laboratories 715-095-150 AB_2340792
Cy™5 AffiniPure Donkey Anti-Mouse IgG (H+L) donkey polyclonal  Jackson ImmunoResearch Laboratories 715-175-150 AB_2340819
Cy™5 AffiniPure Donkey Anti-Rabbit IgG (H+L) donkey polyclonal  Jackson ImmunoResearch Laboratories 711-175-152 AB_2340607
Fluorescein (FITC) AffiniPure Donkey Anti-Rabbit IgG (H+L) donkey polyclonal  Jackson ImmunoResearch Laboratories 711-095-152 AB_2315776
Cy™3 AffiniPure Donkey Anti-Rabbit IgG (H+L) donkey polyclonal  Jackson ImmunoResearch Laboratories 711-165-152 AB_2307443
Fluorescein (FITC) AffiniPure Donkey Anti-Rat IgG (H+L) donkey polyclonal  Jackson ImmunoResearch Laboratories 712-095-153 AB_2340652
Cy™5 AffiniPure Donkey Anti-Rat IgG (H+L) donkey polyclonal  Jackson ImmunoResearch Laboratories 712-175-153 AB_2340672

Validation

All antibodies used are commercially available as described in the manuscript and validated by manufacturer. We selected antibody clones that have been extensively used in the literature. We also titrated all antibodies prior to experiments.  Primary antibodies for flow cytometry purchased from Biolegend are tested by the manufacturer for specificity, by testing of 1-3 target cell types with either single- or multi-color analysis, (including positive and negative cell types). Once specificity is confirmed, each new lot must perform with similar intensity to the in-date reference lot. Brightness (MFI) is evaluated from both positive and negative populations. Each lot product is validated by QC testing with a series of titration dilutions. Purified antibodies are tested for purity by SDS-PAGE gel electrophoresis. Fluorophore and enzyme-conjugated antibodies follow strict manufacturing specifications to ensure performance. Each lot is validated by QC testing as stated on the TDS to confirm specificity and lot-to-lot consistency. Further details can be find at https://www.biolegend.com/en-us/quality/quality-control. The specificity of the secondary antibodies was validated by omission of the primary antibody in the immunoassay. Details for validation of each specific antibody use for flow cytometry or immunofluorescence staining is as follows:

Anti-mouse/human CD11b APC/Cy7 M1/70 rat IgG2b, κ Biolegend AB_830641:
https://www.biolegend.com/de-de/cell-health/apc-cyanine7-anti-mouse-human-cd11b-antibody-3930?GroupID=BLG10616

Anti-mouse CD11c PE/Cy7 N418 Armenian hamster Biolegend AB_493569
https://www.biolegend.com/de-at/explore-new-products/pe-anti-mouse-cd11c-antibody-1816

Anti-mouse CD16/CD32  93 rat IgG2b, λ Biolegend AB_312800
https://www.biolegend.com/en-us/products/ultra-leaf-purified-anti-mouse-cd16-32-antibody-8081?GroupID=BLG6783

Anti-mouse CD172a AF700 P89 Rat IgG1, κ Biolegend AB_2650812
https://www.biolegend.com/fr-ch/explore-new-products/alexa-fluor-700-anti-mouse-cd172a-sirpalpha-antibody-14125

Anti-mouse CD4 F488 RM4-5 rat IgG2a, κ Biolegend AB_493373
https://www.biolegend.com/nl-be/products/fitc-anti-mouse-cd4-antibody-480

Anti-mouse CD45   BV510 30F-11 rat IgG2b, κ Biolegend AB_2561392
https://www.biolegend.com/en-us/punchout/punchout-products/product-detail/brilliant-violet-510-anti-mouse-cd45-antibody-7995?GroupID=BLG1932

Anti-mouse CD45   APC 30F-11 rat IgG2b, κ Biolegend AB_312976
https://www.biolegend.com/en-ie/cell-health/apc-anti-mouse-cd45-antibody-97?GroupID=BLG6837

Anti-mouse CX3CR1 PE SA011F11 rat IgG2a, κ Biolegend AB_2564314
https://www.biolegend.com/en-ie/products/pe-anti-mouse-cx3cr1-antibody-10376?GroupID=BLG13323

Anti-mouse F4/80 PE-Cy5 BM8 rat IgG2a, κ Biolegend AB_893494
https://www.biolegend.com/nl-be/products/pe-anti-mouse-f4-80-antibody-4068

Anti-mouse I-A/I-E BV605 M5/114.15.2 rat IgG2b, κ  Biolegend AB_2565894
https://www.biolegend.com/en-us/punchout/search-results/brilliant-violet-605-anti-mouse-i-a-i-e-antibody-11988?GroupID=BLG11931

Anti-mouse Ly6C FITC HK1.4 rat IgG2c, κ Biolegend AB_1186134
https://www.biolegend.com/en-us/cellular-dyes-and-ancillary-products/fitc-anti-mouse-ly-6c-antibody-4896?GroupID=BLG5853

Anti-mouse Ly6G PerCP/Cy5.5 1A8 rat IgG2a, κ Biolegend AB_1877272
https://www.biolegend.com/ja-jp/products/percp-cyanine5-5-anti-mouse-ly-6g-antibody-6116

Anti-mouse Ly6G APC 1A8 rat IgG2a, κ Biolegend AB_1877163
https://www.biolegend.com/en-us/products/apc-anti-mouse-ly-6g-antibody-6115?GroupID=BLG7234

Anti-mouse TCR β PerCP/Cy5.5 H57-597 Armenian hamster Biolegend AB_1575176
https://www.biolegend.com/en-us/products/percp-cyanine5-5-anti-mouse-tcr-beta-chain-antibody-5603?GroupID=BLG6996

Anti-mouse TER-119 Biotin TER-119 rat IgG2b, κ Biolegend AB_313704
https://www.biolegend.com/fr-ch/products/biotin-anti-mouse-ter-119-erythroid-cells-antibody-1864

Anti-mouse XCR1 PerCP/Cy5.5 ZET mouse IgG2b, κ Biolegend AB_2564363
https://www.biolegend.com/fr-lu/products/percp-cyanine5-5-anti-mouse-rat-xcr1-antibody-10397?Clone=ZET

Anti-mouse CD197 (CCR7) PE 4B12 rat IgG2a, κ Biolegend AB_2564363
https://www.biolegend.com/fr-fr/products/pe-anti-mouse-cd197-ccr7-antibody-2799

Anti-mouse CD209a PE MMD3 mouse IgG2c, κ Biolegend AB_2721636
https://www.biolegend.com/de-de/cell-health/pe-anti-mouse-cd209a-dc-sign-antibody-15353

Anti-mouse CD19 FITC 6D5 rat IgG2a, κ Biolegend AB_313640
https://www.biolegend.com/en-us/cellular-dyes-and-ancillary-products/fitc-anti-mouse-cd19-antibody-1528

Anti-mouse CD3ε FITC 145-2C11 Armenian hamster Biolegend AB_312670
https://www.biolegend.com/en-us/soluble-mhc/fitc-anti-mouse-cd3epsilon-antibody-23

Anti-mouse Ly6G FITC 1A8 rat IgG2a, κ Biolegend AB_1236488
https://www.biolegend.com/en-us/products/fitc-anti-mouse-ly-6g-antibody-4775?GroupID=BLG5803

Anti-mouse K1.1 FITC PK136 mouse IgG2a, κ Biolegend AB_313392
https://www.biolegend.com/en-us/soluble-mhc/fitc-anti-mouse-nk-1-1-antibody-429?GroupID=GROUP20

Anti-mouse TCR β FITC H57-597 Armenian hamster Biolegend AB_313428
https://www.biolegend.com/fr-lu/products/fitc-anti-mouse-tcr-beta-chain-antibody-270?GroupID=BLG6994

Anti-IGF1 mouse Sm1.2 IgG1k, Millipore 05-172:2 is a mouse antibody against IGF-I validated for use in IH, IP, NEUT & WB, and reacts against mouse, rat, chicken and avian species.
https://www.emdmillipore.com/US/en/product/Anti-IGF-I-Antibody-clone-Sm1.2,MM_NF-05-172

Anti-mouse CD206 rat MR5D3 IgG2a BioRad MCA2235, is a rat monoclonal antibody validated for use in C, IF, WB &F.
https://www.bio-rad-antibodies.com/monoclonal/mouse-cd206-antibody-mr5d3-mca2235.html?f=purified#applications

Anti-mouse Iba1 rabbit polyclonal antibody (Wako, 019-19741) is validated for ICC and IHC (Frozen).
https://labchem-wako.fujifilm.com/us/product/detail/W01W0101-1974.html

Anti-DsRed (TdTomato) rabbit polyclonal antibody (Takara, 632496 ) has been raised against DsRed-Express and recognizes tdTomato.
https://www.takarabio.com/documents/Certificate%20of%20Analysis/632496/632496-101717.pdf

Anti-mouse MHC II (I-a/I-E) rat antibody, M5/114  IgG2bk (Millipore, MABF33) is validated for Western Blotting, Flow Cytometry and Immunohistochemistry.
https://www.emdmillipore.com/US/en/product/Anti-MHC-class-II-I-A-I-E-Antibody-clone-M5-114,MM_NF-MABF33#anchor_Description

Fluorescein (FITC) AffiniPure Donkey Anti-Mouse IgG (H+L) donkey polyclonal  Jackson ImmunoResearch Laboratories 715-095-150
Based on immunoelectrophoresis and/or ELISA, the antibody reacts with whole molecule mouse IgG. It also reacts with the light chains of other mouse immunoglobulins. No antibody was detected against non-immunoglobulin serum proteins. The antibody has been tested by ELISA and/or solid-phase adsorbed to ensure minimal cross-reaction with bovine, chicken, goat, guinea pig, syrian hamster, horse, human, rabbit and sheep serum proteins, but it may cross-react with immunoglobulins from other species.
https://www.jacksonimmuno.com/catalog/products/715-095-150/Donkey-Mouse-IgG-HL-Fluorescein-FITC

Cy™5 AffiniPure Donkey Anti-Mouse IgG (H+L) donkey polyclonal  Jackson ImmunoResearch Laboratories 715-175-150
Based on immunoelectrophoresis and/or ELISA, the antibody reacts with whole molecule mouse IgG. It also reacts with the light chains of other mouse immunoglobulins. No antibody was detected against non-immunoglobulin serum proteins. The antibody has been tested by ELISA and/or solid-phase adsorbed to ensure minimal cross-reaction with bovine, chicken, goat, guinea pig, syrian hamster, horse, human, rabbit and sheep serum proteins, but it may cross-react with immunoglobulins from other species.
https://www.jacksonimmuno.com/catalog/products/715-175-150

Cy™5 AffiniPure Donkey Anti-Rabbit IgG (H+L) donkey polyclonal  Jackson ImmunoResearch Laboratories 711-175-152
Based on immunoelectrophoresis and/or ELISA, the antibody reacts with whole molecule rabbit IgG. It also reacts with the light chains of other rabbit immunoglobulins. No antibody was detected against non-immunoglobulin serum proteins. The antibody has been tested by ELISA and/or solid-phase adsorbed to ensure minimal cross-reaction with bovine, chicken, goat, guinea pig, syrian hamster, horse, human, mouse, rat and sheep serum proteins, but it may cross-react with immunoglobulins from other species.
https://www.jacksonimmuno.com/catalog/products/711-005-152

Fluorescein (FITC) AffiniPure Donkey Anti-Rabbit IgG (H+L) donkey polyclonal  Jackson ImmunoResearch Laboratories 711-095-152
Based on immunoelectrophoresis and/or ELISA, the antibody reacts with whole molecule rabbit IgG. It also reacts with the light chains of other rabbit immunoglobulins. No antibody was detected against non-immunoglobulin serum proteins. The antibody has been tested by ELISA and/or solid-phase adsorbed to ensure minimal cross-reaction with bovine, chicken, goat, guinea pig, syrian hamster, horse, human, mouse, rat and sheep serum proteins, but it may cross-react with immunoglobulins from other species.
https://www.jacksonimmuno.com/catalog/products/711-095-152

Cy™3 AffiniPure Donkey Anti-Rabbit IgG (H+L) donkey polyclonal  Jackson ImmunoResearch Laboratories 711-165-152
Based on immunoelectrophoresis and/or ELISA, the antibody reacts with whole molecule rabbit IgG. It also reacts with the light chains of other rabbit immunoglobulins. No antibody was detected against non-immunoglobulin serum proteins. The antibody has been tested by ELISA and/or solid-phase adsorbed to ensure minimal cross-reaction with bovine, chicken, goat, guinea pig, syrian hamster, horse, human, mouse, rat and sheep serum proteins, but it may cross-react with immunoglobulins from other species.
https://www.jacksonimmuno.com/catalog/products/711-165-152

Fluorescein (FITC) AffiniPure Donkey Anti-Rat IgG (H+L) donkey polyclonal  Jackson ImmunoResearch Laboratories 712-095-153

Based on immunoelectrophoresis and/or ELISA, the antibody reacts with whole molecule rat IgG. It also reacts with the light chains of other rat immunoglobulins. No antibody was detected against non-immunoglobulin serum proteins. The antibody has been tested by ELISA and/or solid-phase adsorbed to ensure minimal cross-reaction with bovine, chicken, goat, guinea pig, syrian hamster, horse, human, mouse, rabbit and sheep serum proteins, but it may cross-react with immunoglobulins from other species.
https://www.jacksonimmuno.com/catalog/products/712-095-153

Cy™5 AffiniPure Donkey Anti-Rat IgG (H+L) donkey polyclonal  Jackson ImmunoResearch Laboratories 712-175-153
Based on immunoelectrophoresis and/or ELISA, the antibody reacts with whole molecule rat IgG. It also reacts with the light chains of other rat immunoglobulins. No antibody was detected against non-immunoglobulin serum proteins. The antibody has been tested by ELISA and/or solid-phase adsorbed to ensure minimal cross-reaction with bovine, chicken, goat, guinea pig, syrian hamster, horse, human, mouse, rabbit and sheep serum proteins, but it may cross-react with immunoglobulins from other species.
https://www.jacksonimmuno.com/catalog/products/712-175-153

# Animals and other research organisms

Policy information about studies involving animals; ARRIVE guidelines recommended for reporting animal research, and Sex and Gender in Research

| Laboratory animals | Experiments were performed in young (8-12 week-old) male wild type mice obtained from Jackson Laboratory (IMSR_JAX:000664; Bar Harbor, ME) and aged (17-18 month-old) male and female wild type mice obtained from the NIA-NIH. All in house bred mice were on a C57Bl/6J background and included B6.Cg-Gt(ROSA)26Sortm14(CAG-tdTomato)Hze/J (IMSR_JAX:007914) and B6.129P2(C)-Cx3cr1tm2.1(cre/ERT2)Jung/J (IMSR_JAX:020940). |
|---|---|
| Wild animals | The study did not involve wild animals. |
| Reporting on sex | The sex of animals used for the studies is indicated in table S3. |
| Field-collected samples | The study did not involve field-collected samples. |
| Ethics oversight | All procedures were approved by the institutional animal care and use committee of Weill Cornell Medicine (WCMC IACUC) and were conducted in accordance with the ARRIVE guidelines |

Note that full information on the approval of the study protocol must also be provided in the manuscript.

# Flow Cytometry

## Plots

Confirm that:

☒ The axis labels state the marker and fluorochrome used (e.g. CD4-FITC).

☒ The axis scales are clearly visible. Include numbers along axes only for bottom left plot of group (a 'group' is an analysis of identical markers).

☒ All plots are contour plots with outliers or pseudocolor plots.

☒ A numerical value for number of cells or percentage (with statistics) is provided.

## Methodology

| Sample preparation | Mice were anesthetized with pentobarbital (100 mg/Kg, i.p.) and transcardially perfused with heparinized PBS (2U/ml). Cerebral right cortices were visually inspected after transcardial PBS perfusion to monitor for the presence of ischemic lesion. Briefly, either control-sham or ischemic hemispheres were separated from the cerebellum and olfactory bulb and gently triturated using a Gentle MACS dissociator (Miltenyi Biotec, Auburn, CA). Single cell suspensions were obtained by enzymatic digestion with papain (Neural Tissue Dissociation Kit (P), #130-092-628, Miltenyi Biotec) following the manufacturer's instructions. Four to five hemispheres were pooled for each experiment. In order to increase cell viability and to preserve the transcriptional state during the generation of single-cell suspensions, Brilliant Blue G (BBG, P2X7 receptor antagonist, 1uM, Sigma), AP-5 (25 nM, NMDA receptor blocker, Tocris), and actinomycin D (RNA polymerase inhibitor, 5ug/ml, Sigma) were added to the dissociation solution 142 143. Next, cell suspension was filtered through a 70 um filter, resuspended in 30% Percoll (GE Healthcare)-HBSS containing 1uM BBG, and spun for 10 minutes at 700 g. After gradient centrifugation, the myelin layer was removed, and the cell pellet was resuspended in 2%FBS-PBS buffer and filtered through a 40 um filter. Isolated cells were washed and resuspended in 100 ul of blocking buffer per hemisphere to proceed for FACS staining and cell sorting.<br> For isolation of peripheral leukocytes, mice were anesthetized with pentobarbital (100 mg/Kg, i.p.) and 0.5 ml of blood was collected by cardiac puncture into heparinized tubes. For each experiment the blood from two mice (1 ml total blood) was pooled and erythrocytes were lysed. BBG (1uM) and actinomycin D (5ug/ml) inhibitors were added during the isolation procedure. After erythrolysis, blood cells were resuspended in MACS buffer (PBS supplemented with 2% FBS, 2 mM EDTA; 300 µl/107 cells) and incubated with a biotinylated Ter-119 antibody (Table S2) and remaining erythrocytes were depleted with anti-biotin microbeads according to the manufacturer's instructions (Miltenyi Biotec). Afterward, cells were washed and resuspended in 0.01% BSA-PBS at a concentration of 105 leukocytes/ml for Drop-seq processing.<br><br>Flow Cytometry and Cell Sorting |
|---|---|

For Drop-seq experiments, brain single cell suspensions were incubated with anti-CD16/CD32 antibody for 10 min at 4oC to block Fc receptors, followed by staining with CD45-BV510, Ly6C-FITC, CX3CR1-PE, Ly6G-PercP-Cy5.5 and CD11b-APC-Cy7 antibodies for 15 min at 4oC (Table S2). CD45hi cells, microglia (CD45hiCD11b+CX3CR1+) and endothelial cells (CD45–Ly6C+) were sorted on an Aria II cytometer (BD Bioscience) and collected in 0.5 ml of 0.01% BSA-PBS for Drop-seq. Flow cytometry gating strategy is described in Fig. S1A. Confirmation of brain damage was obtained after evaluating the infiltration of leukocytes in the ischemic brain (Fig. S1B). Analytical flow cytometry was performed on a NovoCyte Flow Cytometer (Agilent, Santa Clara, CA). The antibodies used are described in Table S2. Appropriate isotype controls, 'fluorescence minus one' staining, and staining of negative populations were used to establish gating parameters.

Instrument

NovoCyte Flow Cytometer (Agilent, Santa Clara, CA), Aria II cytometer (BD Bioscience)

Software

NovoExpress flow cytometry software (version 1.6.2) and BD AriaII sorter for data collection and FlowJo™ v10 data analysis

Cell population abundance

The purity was not formally established because the flow sorted cells were used as input for single cell transcriptomisc that allowed for an unbiased de novo cell type assignment.

Gating strategy

To identify CD45hi cells, endothelial cells (EC) and microglia (Mg) in cell suspensions of mouse brains, dead cells and debris were gated out by forward scatter and side scatter properties, and after, doublets were excluded by FSC-Area vs. FSC-Height gating. Live cells (DAPI–) were gated from single cells based on forward and side scatter and DAPI staining. CD45hi and ECs (CD45loLy6Chi) were sorting based on CD45 and Ly6C expression. CD45int was selected for further analysis and examined for the expression of CD11b and CX3CR1 to identify microglia (CD45intCD11b+CX3CR1+). Analysis of CD11b and Ly6G expression was assessed in CD45hi subpopulation to verify the presence of granulocytes (Gran; CD11b+Ly6G+), other myeloid cells, including monocytes derived cells and dendritic cells (MdC/DC; CD11b+Ly6G–) and lymphocytes (CD11b–).

☒ Tick this box to confirm that a figure exemplifying the gating strategy is provided in the Supplementary Information.